

# On the Superlinear Relationship between SGD Noise Covariance and Loss Landscape Curvature

Yikuan Zhang <sup>\*1</sup> Ning Yang <sup>\*2</sup> Yuhai Tu <sup>3</sup>

## Abstract

Stochastic Gradient Descent (SGD) introduces anisotropic noise that is correlated with the local curvature of the loss landscape, thereby biasing optimization toward flat minima. Prior work often assumes an equivalence between the Fisher Information Matrix and the Hessian for negative log-likelihood losses, leading to the claim that the SGD noise covariance  $\mathbf{C}$  is proportional to the Hessian  $\mathbf{H}$ . We show that this assumption holds only under restrictive conditions that are typically violated in deep neural networks. Using the recently discovered Activity-Weight Duality, we find a more general relationship agnostic to the specific loss formulation, showing that  $\mathbf{C} \propto \mathbb{E}_p[\mathbf{h}_p^2]$ , where  $\mathbf{h}_p$  denotes the per-sample Hessian with  $\mathbf{H} = \mathbb{E}_p[\mathbf{h}_p]$ . As a consequence,  $\mathbf{C}$  and  $\mathbf{H}$  commute approximately rather than coincide exactly, and their diagonal elements follow an approximate power-law relation  $C_{ii} \propto H_{ii}^\gamma$  with a theoretically bounded exponent  $1 \leq \gamma \leq 2$ , determined by per-sample Hessian spectra. Experiments across datasets, architectures, and loss functions validate these bounds, providing a unified characterization of the noise-curvature relationship in deep learning.

## 1. Introduction

The remarkable generalizability of Artificial Neural Networks (ANNs) remains one of the central mysteries in deep learning theory (LeCun et al., 2015). The training process, typically driven by Stochastic Gradient Descent (SGD), introduces noise that is not merely an artifact but a crucial feature (Bottou, 1991). It is widely believed that this stochasticity facilitates the escape from sharp minima toward flatter,

<sup>\*</sup>Equal contribution <sup>1</sup>School of Physics, Peking University, Beijing, China <sup>2</sup>Peking University Chengdu Academy for Advanced Interdisciplinary Biotechnologies, Chengdu, China

<sup>3</sup>Flatiron Institute, New York, USA. Correspondence to: Yuhai Tu <ytu@flatironinstitute.org>.

Preprint. February 6, 2026.

more generalizable regions (Hardt et al., 2016; Keskar et al., 2017; Wu et al., 2017; Feng & Tu, 2021; Yang et al., 2023). Crucially, the effectiveness of this process relies on the noise's anisotropy, which stems from alignment between the noise covariance matrix  $\mathbf{C}$  and the loss Hessian  $\mathbf{H}$  (Sagun et al., 2017; 2018; Xing et al., 2018; Nguyen et al., 2019; Chaudhari et al., 2019). Unlike isotropic noise, which is often ineffective in highly degenerate landscapes, this specific geometric coupling acts as the decisive mechanism for driving this geometry-aware exploration (Neelakantan et al., 2015; Zhou et al., 2019; Zhu et al., 2019; Xie et al., 2021a; HaoChen et al., 2021; Yang et al., 2026). A broader review of relevant studies can be found in Appendix A.

Previous studies (Jastrzebski et al., 2018; Zhu et al., 2019; Xie et al., 2021b) have argued that  $\mathbf{C}$  is proportional to  $\mathbf{H}$  near convergence, based on the assumption that the Hessian coincides with the Fisher Information Matrix for cross-entropy (CE). This equivalence, however, requires strong conditions that are frequently violated in modern deep networks (Li et al., 2019). As a result, the Fisher approximation fails to capture the empirically observed anisotropic alignment: it can break down even for cross-entropy loss and is fundamentally inapplicable to mean squared error (MSE). These limitations highlight the need for a more robust framework to accurately characterize the  $\mathbf{C}$ - $\mathbf{H}$  relationship.

In this work, we introduce a new theoretical framework for analyzing the  $\mathbf{C}$ - $\mathbf{H}$  relationship, grounded in the recently discovered Activity-Weight Duality (AWD) (Feng et al., 2023). AWD maps minibatch-induced activity fluctuations—which underlie  $\mathbf{C}$ —onto equivalent weight perturbations in the per-sample loss  $\ell$  that determine  $\mathbf{H}$ . This duality enables us to establish the general  $\mathbf{C}$ - $\mathbf{H}$  relationship regardless of the specific forms of the loss function.

Our main contributions can be summarized as follows:

- We develop a new method to compute the SGD noise covariance  $\mathbf{C}$  based on the Activity-Weight Duality (AWD), which is independent of the specific loss construction, showing that  $\mathbf{C}$  is determined by the second moment of the per-sample Hessian,  $\mathbf{C} \propto \mathbb{E}_p[\mathbf{h}_p^2]$ . Comparing with the definition of the Hessian definition,  $\mathbf{H} = \mathbb{E}_p[\mathbf{h}_p]$ , we claim a superlinear relationship

between  $\mathbf{C}$  and  $\mathbf{H}$ .

- We show empirically that the diagonal entries of  $\mathbf{C}$  exhibits a power-law scaling with those of  $\mathbf{H}$ , i.e.,  $C_{ii} \propto H_{ii}^\gamma$ . While MSE follows an approximately linear scaling ( $\gamma \approx 1$ ), CE loss exhibits a pronounced superlinear scaling ( $\gamma > 1$ ), challenging the classical Fisher approximation. Building on the AWD framework, we further prove that the scaling exponent is universally bounded as  $1 \leq \gamma \leq 2$ .
- We uncover the geometric origins of the distinction in  $\gamma$  between CE ( $\gamma > 1$ ) and MSE ( $\gamma \approx 1$ ) via a “suppression experiment”. While both losses exhibit per-sample Hessians dominated by a single leading eigenvalue, CE displays a strong positive correlation between the magnitude of this eigenvalue and its alignment with global Hessian directions, leading to  $\gamma > 1$ , whereas these quantities are effectively independent for MSE, yielding  $\gamma \rightarrow 1$ . This eigenvalue–eigendirection entanglement provides a geometric explanation for the observed superlinear scaling in CE.

## 2. Background and Motivation

### 2.1. The Flaw in Fisher Approximation

SGD updates model parameters using stochastic gradients estimated from randomly sampled mini-batches (Robbins & Monro, 1951; Bottou, 1991). Let  $\mathcal{D} = \{(\mathbf{x}_i, y_i)\}_{i=1}^N$  denote the training set of size  $N$ . At iteration  $t$ , a mini-batch  $\mathcal{B}_{\mu_t}$  of size  $B$  is sampled uniformly from  $\mathcal{D}$ . The parameters  $\mathbf{w}_t$  are updated with a learning rate  $\eta$  as:

$$\mathbf{w}_{t+1} = \mathbf{w}_t - \eta \nabla \mathcal{L}^{\mu_t}(\mathbf{w}_t), \quad (1)$$

where  $\mathcal{L}^{\mu_t}(\mathbf{w}_t)$  represents the mini-batch loss. Conceptually, the SGD noise arises from the deviation of the local mini-batch gradient from the full-batch gradient  $\mathbf{g}(\mathbf{w}_t) \triangleq \nabla \mathcal{L}(\mathbf{w}_t)$ , where  $\mathcal{L}(\mathbf{w}_t)$  denotes the empirical risk over the entire dataset.

Assuming the mini-batch size  $B$  is sufficiently large for the central limit theorem to hold, the stochastic gradient is well-approximated by a Gaussian distribution (Mandt et al., 2017; Smith & Le, 2018; Chaudhari & Soatto, 2018; Xie et al., 2021b):  $\nabla \mathcal{L}^{\mu}(\mathbf{w}) \sim \mathcal{N}(\mathbf{g}(\mathbf{w}), \mathbf{C}(\mathbf{w}))$ . Since samples are drawn independent and identically distributed (i.i.d.) from the finite dataset, the noise covariance matrix  $\mathbf{C}(\mathbf{w})$  scales with the covariance of the per-sample gradients (Smith & Le, 2018):

$$\begin{aligned} \mathbf{C}(\mathbf{w}) &= \frac{1}{B} \left[ \frac{1}{N} \sum_{i=1}^N \nabla \ell_i(\mathbf{w}) \nabla \ell_i(\mathbf{w})^\top - \mathbf{g}(\mathbf{w}) \mathbf{g}(\mathbf{w})^\top \right] \\ &\approx \frac{1}{BN} \sum_{i=1}^N \nabla \ell_i(\mathbf{w}) \nabla \ell_i(\mathbf{w})^\top. \end{aligned} \quad (2)$$

Here, we use the shorthand  $\ell_i(\mathbf{w}) \triangleq \ell(\mathbf{x}_i, y_i; \mathbf{w})$  to represent the per-sample loss. The approximation in Eq. (2) assumes the training has converged to a vicinity of a local minimum where the gradient magnitude is negligible, i.e.,  $\|\mathbf{g}(\mathbf{w})\| \approx 0$ . Consequently, the noise covariance is dominated by the uncentered second moment of the gradients.

For probabilistic models trained with the negative log-likelihood loss (e.g., cross-entropy), defined as  $\ell(\mathbf{x}, y; \mathbf{w}) = -\log p_{\mathbf{w}}(y|\mathbf{x})$ , the noise covariance relates closely to the geometry of the loss landscape. The Hessian of the total loss,  $\mathbf{H}(\mathbf{w}) = \nabla^2 \mathcal{L}(\mathbf{w})$ , can be decomposed as:

$$\begin{aligned} \mathbf{H}(\mathbf{w}) &= \frac{1}{N} \sum_{i=1}^N \nabla \log p_{\mathbf{w}}(y_i|\mathbf{x}_i) \nabla \log p_{\mathbf{w}}(y_i|\mathbf{x}_i)^\top \\ &\quad - \frac{1}{N} \sum_{i=1}^N \frac{1}{p_{\mathbf{w}}(y_i|\mathbf{x}_i)} \nabla^2 p_{\mathbf{w}}(y_i|\mathbf{x}_i). \end{aligned} \quad (3)$$

The first term corresponds to the empirical Fisher information matrix ( $\mathbf{F}$ ). Under the realizability assumption—where the model distribution  $p_{\mathbf{w}}(y|\mathbf{x})$  coincides with the true data-generating distribution  $p_{\text{data}}(y|\mathbf{x})$ —the second term vanishes in expectation at the optimum (Jastrzebski et al., 2018; Zhu et al., 2019; Xie et al., 2021b). Specifically, if there exists  $\mathbf{w}^*$  such that  $p_{\mathbf{w}^*}(y|\mathbf{x}) = p_{\text{data}}(y|\mathbf{x})$ , the expected value of the second term becomes:

$$\begin{aligned} &\mathbb{E}_{\mathbf{x}, y \sim p_{\text{data}}} \left[ \frac{1}{p_{\mathbf{w}^*}(y|\mathbf{x})} \nabla^2 p_{\mathbf{w}^*}(y|\mathbf{x}) \right] \\ &= \int p(\mathbf{x}) \left[ \int p_{\text{data}}(y|\mathbf{x}) \frac{1}{p_{\mathbf{w}^*}(y|\mathbf{x})} \nabla^2 p_{\mathbf{w}^*}(y|\mathbf{x}) \, dy \right] \, d\mathbf{x} \\ &= \int p(\mathbf{x}) \nabla^2 \left[ \int p_{\mathbf{w}^*}(y|\mathbf{x}) \, dy \right] \, d\mathbf{x} = 0, \end{aligned} \quad (4)$$

where the simplification follows the normalization condition  $\int p_{\mathbf{w}^*}(y|\mathbf{x}) \, dy = 1$ . Under these conditions, the Hessian equals the Fisher information matrix ( $\mathbf{H} \approx \mathbf{F}$ ), leading to the approximation  $\mathbf{C} \propto \mathbf{H}$ .

Although theoretically appealing, this argument relies on assumptions that are seldom satisfied in deep learning practice (Li et al., 2019). Beyond its restriction to negative log-likelihood losses, it exhibits two additional limitations. First, it assumes likelihood smoothness ( $C^2$  continuity) to interchange differentiation and integration. This regularity is violated by common non-smooth components like ReLU activations and max-pooling operations. Second, and more critically, the approximation fails under deterministic supervision. The vanishing of the second Hessian term relies on the expectation being taken over the model distribution. However, real-world data distributions are typically Dirac deltas:

$$p_{\text{data}}(y|\mathbf{x}) = \delta(y - y^*(\mathbf{x})), \quad (5)$$

where  $y^*(\mathbf{x})$  is the ground-truth label. Under this distribution, the expectation collapses to a single point evaluation rather than an integral over the the label space, preventing the cancellation mechanism from functioning.

## 2.2. Commutativity between $\mathbf{C}$ and $\mathbf{H}$

Beyond the failure of statistical assumptions, the violation of a direct linear relation between  $\mathbf{C}$  and  $\mathbf{H}$  can be seen by dimensional analysis. The loss function  $\mathcal{L}$  carries an intrinsic physical dimension (e.g., squared error units or bits). Consequently, the elements of the Hessian  $\mathbf{H}$  possess dimensions of  $[\mathcal{L}]/[\mathbf{w}]^2$ , whereas the covariance matrix  $\mathbf{C}$  scales as  $[\mathcal{L}]^2/[\mathbf{w}]^2$ . Thus, the hypothesized proportionality  $\mathbf{C} \propto \mathbf{H}$  is dimensionally inconsistent. Any strict linear relationship would require a proportionality constant with dimensions of  $[\mathcal{L}]$ , implying that the relationship depends on the arbitrary scale of the loss function.

Given the dimensional mismatch that rules out strict linear dependence, we investigate a weaker condition: do  $\mathbf{C}$  and  $\mathbf{H}$  share the same eigensystem? This is equivalent to checking matrix commutativity. We analyze the structure of  $\mathbf{C}$  in the eigenbasis of  $\mathbf{H}$ . As visualized in Figure 1(a),  $\mathbf{C}$  exhibits a characteristic “arrowhead” structure: the diagonal is dominant, but non-negligible off-diagonal elements persist in the top rows and columns.

However, large eigenvalues tend to overshadow the structure of the bulk spectrum. To separate geometric alignment from these magnitude effects, we use the scale-invariant correlation matrix  $\mathbf{R}$ , defined as:

$$R_{ij} = \frac{C_{ij}}{\sqrt{|C_{ii}C_{jj}|}}. \quad (6)$$

Here, the diagonal elements  $R_{ii}$  are unity, while off-diagonal terms  $R_{ij}$  quantify the relative coupling strength between eigen-directions  $i$  and  $j$ .

To rigorously benchmark this alignment, we construct a randomized baseline  $\mathbf{R}_{\text{rand}}$ . This baseline is generated by rotating  $\mathbf{C}$  with a random orthogonal matrix  $\mathbf{Q}$  before projecting it onto the Hessian basis ( $\mathbf{C}_{\text{rand}} = \mathbf{Q}\Lambda_C\mathbf{Q}^\top$ ). This procedure preserves the eigenvalue spectrum of  $\mathbf{C}$  while destroying any specific geometric alignment with  $\mathbf{H}$ .

The results reveal a strong structural alignment between the noise covariance and the Hessian. As shown in Figure 1(b), the real correlation matrix  $\mathbf{R}_{\text{real}}$  is sharply concentrated along the diagonal, in contrast to the random baseline  $\mathbf{R}_{\text{rand}}$  with significant off-diagonal elements (Figure 1(c)). We quantify this effect using the mean off-diagonal elements:

$$\mu = \mathbb{E}_{i \neq j} [|R_{ij}|]. \quad (7)$$

For a heavy-tailed spectrum with  $M$  dominant eigenvalues (Sagun et al., 2017; 2018; Tang et al., 2025), the

Random Matrix Theory predicts a background level of  $\mu_{\text{rand}} \approx 0.8/\sqrt{M}$  (see derivation in Appendix C). In our case (CNN on CIFAR-10), the “arrowhead” structure suggests an effective bandwidth of  $M \approx 20$ , implying a relatively high theoretical noise floor ( $\mu_{\text{rand}} \approx 0.2$ ). However, the observed mean off-diagonal elements  $\mu_{\text{real}} \approx 0.066$  is significantly smaller (P-value  $p \ll 10^{-50}$ , see Appendix D), which provides statistical evidence that the noise covariance matrix  $\mathbf{C}$  is highly aligned with the Hessian  $\mathbf{H}$ .

In the following section (Theorem 3.4 and Appendix E.2), we provide an analytical argument showing that the off-diagonal elements  $C_{ij}$  ( $i \neq j$ ) are asymptotically negligible. This is consistent with the numerical results in Figures 7 to 9 (last row), and further implies that  $\mathbf{C}$  and  $\mathbf{H}$  approximately commute, i.e.,  $[\mathbf{C}, \mathbf{H}] \approx 0$ .

## 3. C-H Relation via Activity-Weight Duality

To overcome the inherent limitations of the Fisher approximation, we utilize the Activity-Weight Duality (AWD) framework proposed by (Feng et al., 2023). AWD establishes an exact correspondence between changes in the activity space due to variations in data and equivalent perturbations in the weight space, independent of the specific loss formulation.

### 3.1. Matched Sample Pairs and Perturbations

To isolate the SGD noise arising from intra-class variance, we construct a mapping between samples in two sequential mini-batches,  $\mathcal{B}_\mu$  and  $\mathcal{B}_\nu$ . Assuming balanced mini-batches, we establish a one-to-one correspondence where every sample  $p \in \mathcal{B}_\nu$  is paired with a unique partner  $p' \in \mathcal{B}_\mu$  based on class identity and geometric proximity (Feng et al., 2023). Specifically, for a sample  $p$  with input  $\mathbf{x}_p$ , its partner  $p'$  is identified as:  $p' = \arg \min_{k \in \mathcal{B}_\mu, y_k = y_p} \|\mathbf{x}_k - \mathbf{x}_p\|_2$ . This pairing strategy ensures that the activity perturbation  $\Delta \mathbf{a}_p = \mathbf{a}_{p'} - \mathbf{a}_p$  captures the minimal variance intrinsic to the data manifold, filtering out inter-class variability. We extend this logic to the entire batch, treating the SGD noise as the aggregate of these microscopic pairwise dualities.

### 3.2. Minimal Activity-Weight Duality in FCL

For a single Fully Connected Layer (FCL) parameterized by weights  $\mathbf{W} \in \mathbb{R}^{d_{\text{out}} \times d_{\text{in}}}$ . Let  $\mathbf{a} \in \mathbb{R}^{d_{\text{in}}}$  be the input activity.

**Definition 3.1** (Minimal Activity-Weight Duality (Feng et al., 2023)). Given an input activity perturbation  $\Delta \mathbf{a}$  derived from a matched sample pair, the Minimal Activity-Weight Duality defines the unique weight perturbation  $\Delta \mathbf{W}^*$  that satisfies the condition of invariant pre-activation  $\mathbf{W}(\mathbf{a} + \Delta \mathbf{a}) = (\mathbf{W} + \Delta \mathbf{W})\mathbf{a}$ , while minimizing the Frobe-

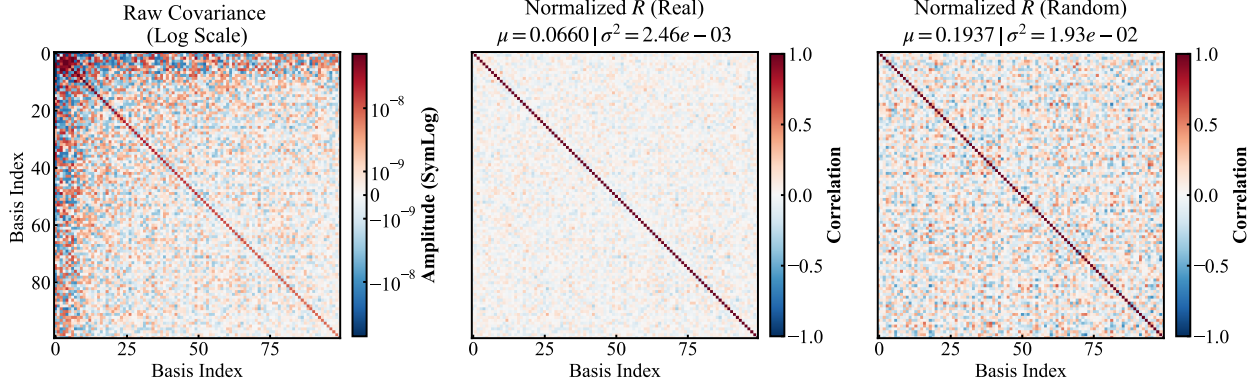


Figure 1. Noise–curvature alignment for a CNN trained on CIFAR-10 with cross-entropy loss (top 100 eigen-directions). (a) The empirical covariance matrix  $\mathbf{C}$  represented in the Hessian eigenbasis. (b) The scale-invariant correlation matrix  $\mathbf{R}_{\text{real}}$ , normalized by diagonal elements. (c) The randomized Baseline  $\mathbf{R}_{\text{rand}}$ , constructed by randomly rotating  $\mathbf{C}$  while preserving its eigenvalue spectrum. See Appendix Figures 7 to 9 for more details and results on additional architectures.

nious norm of the weight change:

$$\begin{aligned} \Delta \mathbf{W}^* &= \arg \min_{\Delta \mathbf{W}} \|\Delta \mathbf{W}\|_F^2 \\ \text{s.t. } \Delta \mathbf{W} \mathbf{a} &= \mathbf{W} \Delta \mathbf{a}. \end{aligned} \quad (8)$$

As a consequence, the per-sample loss remains invariant, i.e.,  $\ell(\mathbf{x}_{p'}; \mathbf{W}) = \ell(\mathbf{x}_p; \mathbf{W} + \Delta \mathbf{W})$ . The constraint implies that the shift in the weight space must reproduce the exact shift in the pre-activation space caused by the activity noise.

**Lemma 3.2** (Explicit Solution for AWD (Feng et al., 2023)). *The closed-form solution to the optimization problem in Definition 3.1 is a rank-1 outer product given by:*

$$\Delta \mathbf{W}^* = \frac{(\mathbf{W} \Delta \mathbf{a}) \mathbf{a}^\top}{\|\mathbf{a}\|^2}. \quad (9)$$

We provide the proof in Appendix E.1. Intuitively, Eq. (9) demonstrates that the equivalent weight noise  $\Delta \mathbf{W}^*$  is aligned with the outer product of the propagated error  $\mathbf{W} \Delta \mathbf{a}$  and the input activation  $\mathbf{a}$ . Note that for the subsequent gradient analysis, we denote the vectorized weights as  $\mathbf{w} = \text{vec}(\mathbf{W}) \in \mathbb{R}^D$ .

### 3.3. AWD-Based Gradient Approximation

Let  $\mathcal{L}^\mu$  and  $\mathcal{L}^\nu$  denote the empirical losses on two sequential mini-batches  $\mu$  and  $\nu$ . The SGD noise covariance  $\mathbf{C}$  is defined as the expectation of the outer product of the gradient difference  $\mathbf{C} = \frac{1}{2} \mathbb{E}_{\mu, \nu} [\mathbf{g}_{\mu\nu} \mathbf{g}_{\mu\nu}^\top]$ , where  $\mathbf{g}_{\mu\nu} \triangleq \nabla \mathcal{L}^\nu(\mathbf{w}) - \nabla \mathcal{L}^\mu(\mathbf{w})$ . To establish a tractable link between the SGD noise and the Hessian, we first analyze the asymptotic behavior of  $\mathbf{g}_{\mu\nu}$ . Our main result posits that in the vicinity of a local minimum, the noise structure is dominated by the loss curvature.

**Lemma 3.3** (AWD Gradient Approximation). *Under the assumption that the training is near a local minimum where the*

gradient magnitude is negligible relative to the curvature-induced shift (i.e.,  $\|\nabla \ell\| \ll \|\mathbf{h} \Delta \mathbf{w}\|$ ),  $\mathbf{g}_{\mu\nu}$  is dominated by the Hessian-driven term:

$$\mathbf{g}_{\mu\nu} \approx \frac{1}{B} \sum_{p \in \mathcal{B}_\nu} \mathbf{h}_p(\mathbf{w}) \Delta \mathbf{w}_p^{\mu\nu}. \quad (10)$$

*Proof.* We utilize the AWD framework to bridge the gap between the two batches. Specifically, we treat a sample  $p' \in \mathcal{B}_\mu$  as a perturbed version of its partner  $p \in \mathcal{B}_\nu$ . Let  $\Delta \mathbf{w}_p^{\mu\nu}$  denote the minimal weight perturbation (from Lemma 3.2) mapping sample  $p$  to  $p'$ . Approximating the gradient  $\nabla \ell_{p'}$  via a first-order Taylor expansion around the perturbed weights of sample  $p$  gives:

$$\begin{aligned} \nabla \ell_p(\mathbf{w}) - \nabla \ell_{p'}(\mathbf{w}) &\approx \nabla \ell_p(\mathbf{w}) - \nabla \ell_p(\mathbf{w} + \Delta \mathbf{w}_p^{\mu\nu}) \\ &\approx -\nabla^2 \ell_p(\mathbf{w}) \Delta \mathbf{w}_p^{\mu\nu} \\ &\quad - (\nabla \Delta \mathbf{w}_p^{\mu\nu})^\top \nabla \ell_p(\mathbf{w}). \end{aligned} \quad (11)$$

Summing over the mini-batch yields:

$$\mathbf{g}_{\mu\nu} \approx \frac{1}{B} \sum_{p \in \mathcal{B}_\nu} \left[ \underbrace{\mathbf{h}_p(\mathbf{w}) \Delta \mathbf{w}_p^{\mu\nu}}_{\text{Term I}} + \underbrace{(\nabla \Delta \mathbf{w}_p^{\mu\nu})^\top \nabla \ell_p(\mathbf{w})}_{\text{Term II}} \right]. \quad (12)$$

As visualized in Figures 4 and 6 (f&g), near a global minimum,  $\|\nabla \ell\| \rightarrow 0$  while the curvature  $\mathbf{h}_p$  remains significant. Consequently, Term II decays faster than Term I, recovering Eq. (10). Detailed validation is in Appendix E.2.  $\square$

### 3.4. Spectral Structure of the Noise Covariance

Substituting the approximation from Lemma 3.3 into the definition of  $\mathbf{C}$ , and assuming that cross-terms between distinct samples vanish due to i.i.d. sampling, the covariance

reduces to a quadratic form of the per-sample Hessian:

$$\mathbf{C} \approx \frac{1}{2B} \mathbb{E}_p [\mathbf{h}_p(\mathbf{w}) \mathcal{M}_p \mathbf{h}_p(\mathbf{w})], \quad (13)$$

where  $\mathcal{M}_p = \mathbb{E}_\mu [\Delta \mathbf{w}_p^\mu \Delta \mathbf{w}_p^{\mu \top}]$  is the variance of weight perturbations. The prefactor scales as  $1/(2B)$  after aggregating independent sample contributions.

Comparing this result with the definition of the Hessian  $\mathbf{H} = \mathbb{E}_p[\mathbf{h}_p]$  reveals a fundamental structural distinction:  $\mathbf{H}$  is the linear average (first moment) of the curvature, whereas  $\mathbf{C}$  depends on the quadratic form (second moment) of the curvature.

**Spectral Decomposition.** To quantify this relationship, we analyze  $\mathbf{C}$  and  $\mathbf{H}$  in the global eigenbasis  $\{\mathbf{v}_i\}$  of  $\mathbf{H}$  where  $\mathbf{H}\mathbf{v}_i = H_{ii}\mathbf{v}_i$ . We also utilize the local eigenbasis  $\{\mathbf{u}_m^{(p)}\}$  of the per-sample Hessian  $\mathbf{h}_p$  (where  $\mathbf{h}_p \mathbf{u}_m^{(p)} = \kappa_m^{(p)} \mathbf{u}_m^{(p)}$ ).

**Theorem 3.4** (Spectral Decomposition of SGD Noise). *Under the AWD Gradient Approximation and assuming sample independence, if the covariance of per-sample weight perturbations in its local eigenbasis is isotropic and uniform across different samples:*

$$\mathcal{M}_{p,mn} = \mathbb{E}_\mu [(\mathbf{u}_m^{(p)})^\top \Delta \mathbf{w}_p^\mu (\Delta \mathbf{w}_p^\mu)^\top \mathbf{u}_n^{(p)}] \approx \sigma_w^2 \delta_{mn}, \quad (14)$$

where  $\sigma_w^2$  denotes the weight perturbation variance, the covariance matrix element  $C_{ij} = \mathbf{v}_i^\top \mathbf{C} \mathbf{v}_j$  is given by:

$$C_{ij} \approx \frac{\sigma_w^2}{2B} \mathbb{E}_p \left[ \sum_m (\kappa_m^{(p)})^2 (\mathbf{u}_m^{(p)} \cdot \mathbf{v}_i) (\mathbf{u}_m^{(p)} \cdot \mathbf{v}_j) \right]. \quad (15)$$

(Proof provided in [Appendix E.2.3](#).)

**Remark 3.5.** Statistically, for the off-diagonal elements  $C_{ij}$ , the terms  $\mathbf{u}_m^{(p)} \cdot \mathbf{v}_{i(j)}$  can be interpreted as the projections of a random vector  $\mathbf{u}_m^{(p)}$  onto two orthogonal directions  $\mathbf{v}_i$  and  $\mathbf{v}_j$ . In the extremely high-dimensional regime ( $N \sim 2000$ ) with on the order of  $\sim 20,000$  samples, these projections are effectively independent and have nearly zero mean. Consequently, the off-diagonal entries  $C_{ij}$  vanish asymptotically, consistent with the numerical observations in [Figures 7 to 9](#) (last row).

**Remark 3.6 (Dimensional Consistency).** This result naturally resolves the dimensional inconsistency discussed in [Section 2.2](#). The noise variance  $C_{ij}$  (dimension  $[\mathcal{L}]^2/[\mathbf{w}]^2$ ) is expressed as the product of squared curvature  $(\kappa_m^{(p)})^2$  (dimension  $[\mathcal{L}]^2/[\mathbf{w}]^4$ ) and weight variance  $\sigma_w^2$  (dimension  $[\mathbf{w}]^2$ ). The resulting dimensions match perfectly without arbitrary constants.

**Origin of Superlinear C–H relationship.** Equation (15) elucidates the microscopic mechanism underlying the relationship between SGD noise and loss landscape curvature. It reveals

that the noise strength  $C_{ii}$  along a given global Hessian eigen-direction  $\mathbf{v}_i$  is determined by the interplay of two local factors: 1. Local curvature magnitude: the contribution of spectral outliers that dominate the local eigenvalues  $\kappa_m^{(p)}$ , corresponding to “stiff” modes ([Sagun et al., 2017; 2018; Wu et al., 2017; Popyan, 2019b;a](#)); and 2. Local-global alignment: the degree of overlap between the local principal directions  $\mathbf{u}_m^{(p)}$  with these stiff samples and the global direction  $\mathbf{v}_i$ .

The emergence of superlinear scaling arises directly from the statistical distinction between the global Hessian and the noise covariance. The global Hessian eigenvalue  $H_{ii}$  represents the first moment of the projected local curvatures:

$$H_{ii} = \mathbf{v}_i^\top \mathbf{H} \mathbf{v}_i = \mathbb{E}_p \left[ \sum_m \kappa_m^{(p)} (\mathbf{u}_m^{(p)} \cdot \mathbf{v}_i)^2 \right]. \quad (16)$$

In contrast, [Theorem 3.4](#) establishes that the noise covariance scales with the second moment:

$$C_{ii} \propto \mathbb{E}_p \left[ \sum_m (\kappa_m^{(p)})^2 (\mathbf{u}_m^{(p)} \cdot \mathbf{v}_i)^2 \right]. \quad (17)$$

Previous studies have demonstrated that the spectra of both the Hessian and Covariance follow a “bulk-and-outlier” structure characterized by heavy-tailed, power-law decay ([Xie et al., 2023; Tang et al., 2025](#)). In this heavy-tailed regime, the dependence on the second moment significantly accelerates the spectral decay rate of the Covariance relative to the Hessian, manifesting as a superlinear relationship.

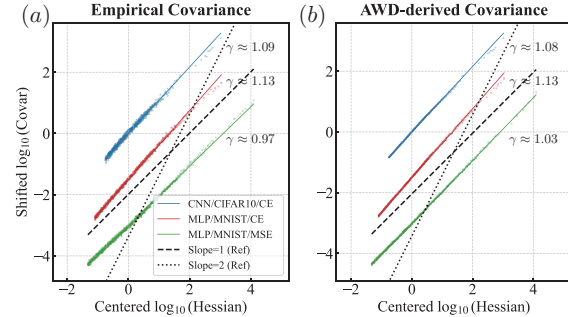


**Figure 2.** Log-log plot of diagonal elements using the top 1000 eigenvalues for models trained to convergence (100% training accuracy for CE and  $> 95\%$  for MSE). Data points are mean-centered and vertically shifted for visualization; solid lines denote linear fits. (a) Empirical noise covariance versus the Hessian. (b) AWD-derived noise covariance (Eq. 15) versus the Hessian. The dotted and dashed lines correspond to slope 1 and 2, respectively.

## 4. Empirical Power-Law

To quantify the superlinear relation, we plot  $C_{ii}$  versus  $H_{ii}$  in the log-log scale. As shown in [Figure 2\(a\)](#), the results can be fitted by a simple linear line with slope  $\gamma$ , consistent with previous observations ([Xie et al., 2023; Tang et al.,](#)

2025). Note that we estimate  $\gamma$  using the top 1000 dominant eigenvalues, avoiding the degenerate tail of the Hessian spectrum to ensure numerical stability (Meurant & Strakoš, 2006; Yao et al., 2019; Tang et al., 2025).

As shown in Figure 2(b) (with additional results in Figures 10 to 12), the empirical power-law relationship,

$$C_{ii} \propto H_{ii}^\gamma, \quad (18)$$

also applies to our theoretical results based on AWD with similar exponents.

Table 1 provides a quantitative comparison between the scaling exponent  $\gamma_{\text{emp}}$ , measured from the full covariance  $\mathbf{C}$  computed via Eq. 2, and the exponent  $\gamma_{\text{AWD}}$  obtained from the approximate covariance derived using AWD (Eq. 15). The comparison spans different models and datasets, as well as two loss functions, cross-entropy (CE) and mean-squared error (MSE). All models trained with CE loss are run to convergence and achieve 100% training accuracy. In contrast, for MSE loss, only  $> 95\%$  training accuracy is attained within the same training time, reflecting the weaker convergence behavior of the quadratic loss.

For the CE loss, the AWD-predicted exponent  $\gamma_{\text{AWD}}$  closely matches the empirical exponent  $\gamma_{\text{emp}}$  and is significantly larger than unity, reaching values as high as  $\gamma \approx 1.4$ . In contrast, for the MSE loss,  $\gamma_{\text{emp}}$  is consistently smaller than that observed for CE and remains close to  $\gamma \approx 1$ . A closer examination reveals a slight deviation between  $\gamma_{\text{AWD}}$  and  $\gamma_{\text{emp}}$ , which can be attributed to the non-vanishing gradient norm  $\|\nabla \ell\|$ . This residual gradient weakens the condition  $\|\nabla \ell\| \ll \|\mathbf{h} \Delta \mathbf{w}\|$  underlying the AWD gradient approximation (Lemma 3.3). Indeed, incorporating the second term in Eq. 12 improves the agreement between  $\gamma_{\text{emp}}$  and  $\gamma_{\text{AWD}}$ , as demonstrated in Appendix B.2.2.

**Table 1.** Comparison of the scaling exponent  $\gamma$  between empirical measurements ( $\gamma_{\text{emp}}$ ) and AWD-based theoretical predictions ( $\gamma_{\text{AWD}}$ ). Experiments were conducted on MNIST and CIFAR-10 datasets ( $C$  denotes the number of classes used) using MLP and CNN architectures. Values represent the mean  $\pm$  standard deviation over 4 independent runs.

DATA	MODEL	$C$	MSE		CE	
			$\gamma_{\text{emp}}$	$\gamma_{\text{AWD}}$	$\gamma_{\text{emp}}$	$\gamma_{\text{AWD}}$
MNIST	MLP	3	1.07 $\pm$ 0.02	1.14 $\pm$ 0.02	1.22 $\pm$ 0.01	1.24 $\pm$ 0.01
		6	1.01 $\pm$ 0.01	1.08 $\pm$ 0.01	1.19 $\pm$ 0.01	1.19 $\pm$ 0.01
		10	0.96 $\pm$ 0.01	1.03 $\pm$ 0.01	1.14 $\pm$ 0.01	1.14 $\pm$ 0.01
	CNN	3	0.99 $\pm$ 0.01	1.05 $\pm$ 0.02	1.38 $\pm$ 0.05	1.33 $\pm$ 0.03
		6	1.03 $\pm$ 0.01	1.06 $\pm$ 0.01	1.33 $\pm$ 0.01	1.31 $\pm$ 0.01
		10	0.98 $\pm$ 0.01	1.05 $\pm$ 0.01	1.31 $\pm$ 0.02	1.29 $\pm$ 0.02
CIFAR-10	MLP	3	1.12 $\pm$ 0.04	1.17 $\pm$ 0.03	1.27 $\pm$ 0.04	1.27 $\pm$ 0.04
		6	1.03 $\pm$ 0.01	1.08 $\pm$ 0.02	1.43 $\pm$ 0.01	1.43 $\pm$ 0.01
		10	1.00 $\pm$ 0.02	1.03 $\pm$ 0.02	1.51 $\pm$ 0.03	1.47 $\pm$ 0.03
	CNN	3	1.04 $\pm$ 0.04	1.09 $\pm$ 0.03	1.10 $\pm$ 0.01	1.11 $\pm$ 0.01
		6	1.00 $\pm$ 0.01	1.01 $\pm$ 0.01	1.08 $\pm$ 0.02	1.08 $\pm$ 0.01
		10	1.01 $\pm$ 0.01	1.02 $\pm$ 0.01	1.08 $\pm$ 0.01	1.08 $\pm$ 0.01

The empirical analysis reveals a critical divergence: while MSE yields  $\gamma \approx 1$ , CE consistently exhibits superlinear

scaling  $\gamma > 1$ . This behavior stands in direct contradiction to the Fisher approximation, which predicts strict linearity for negative log-likelihood losses (Jastrzebski et al., 2018; Zhu et al., 2019; Xie et al., 2021b).

## 5. Universal Bounds on the Scaling Exponent

### 5.1. Derivation of the Bounds

To provide a theoretical foundation for the observed superlinear scaling, we establish universal bounds  $1 \leq \gamma \leq 2$  derived from Theorem 3.4. Our analysis focuses on the vicinity of local minima, where these bounds can be established rigorously. While this approach relies on local convexity in the late stage of training, it avoids the restrictive “true parameter” assumption inherent in the Fisher approximation. This distinction is essential: in the highly non-convex landscapes of deep neural networks, convergence to a generic local minimum is a realistic outcome of training, whereas exact realizability is rarely guaranteed (Liu et al., 2020; Sun et al., 2020; Liu et al., 2022; Zhang et al., 2022).

**Theorem 5.1** (Universal Bounds on  $\gamma$ ). *Consider the loss landscape in the vicinity of a local minimum  $\mathbf{w}^*$  where local convexity holds, i.e., the per-sample Hessians  $\mathbf{h}_p(\mathbf{w}^*)$  are positive semi-definite (PSD). Let  $\kappa_{\text{max}}$  be the uniform upper bound of the per-sample eigenvalues. Then, the following properties hold:*

1. *The diagonal elements of the noise covariance are bounded by the linear and quadratic forms of the Hessian:*

$$\frac{\sigma_w^2}{2B} H_{ii}^2 \leq C_{ii} \leq \frac{\sigma_w^2 \kappa_{\text{max}}}{2B} H_{ii}. \quad (19)$$

2. *Consequently, for an empirical power-law relationship  $C_{ii} \propto H_{ii}^\gamma$ , the scaling exponent  $\gamma$  is theoretically bounded by:*

$$1 \leq \gamma \leq 2. \quad (20)$$

We defer the detailed proof to Appendix E.3.

**Remark 5.2** (Empirical Robustness Beyond Local Convexity). Although Theorem 5.1 is derived under the assumption of positive curvature at local minima, empirical results (Figures 4 to 6) show that the scaling law  $\gamma \in [1, 2]$  emerges much earlier, well before convergence. This suggests that noise-curvature alignment is an intrinsic property of SGD, persisting even in training regimes where the Fisher approximation—relying on asymptotic realizability—fails to hold.

### 5.2. Physical Interpretation

To provide an intuitive interpretation of the scaling exponent  $\gamma$ , we examine the conditions under which the theoretical bounds  $1 \leq \gamma \leq 2$  can be realized. Recall from Theorem 3.4 that  $\gamma$  essentially quantifies the relationship between the

first moment ( $\mathbf{H}$ ) and the second moment ( $\mathbf{C}$ ) of the local curvature spectrum. This relationship is governed by the interplay between the local curvature magnitudes  $\kappa_m^{(p)}$  and their projections onto the global eigenbasis  $(\mathbf{u}_m^{(p)} \cdot \mathbf{v}_i)^2$ . We identify two distinct limiting cases:

**Proposition 5.3** (Perfect Alignment,  $\gamma \rightarrow 2$ ). *Consider an idealized scenario of perfect geometric alignment, where local eigenbases align strictly with the global eigenbasis  $((\mathbf{u}_m^{(p)} \cdot \mathbf{v}_i)^2 = \delta_{mi})$ , but the curvature magnitudes  $\kappa_i^{(p)}$  fluctuate stochastically. If  $\text{Var}_p(\kappa_i^{(p)}) \propto (\mathbb{E}_p[\kappa_i^{(p)}])^2$ , then the second moment scales quadratically with the Hessian:*

$$C_{ii} \propto H_{ii}^2 \implies \gamma = 2. \quad (21)$$

**Remark 5.4** (Theoretical Upper Bound). The limit  $\gamma \rightarrow 2$  implies a landscape where every sample's curvature aligns perfectly with the global structure. While the toy ‘‘Random Shifts Model’’ (Yang et al., 2023) provides a theoretical instance of this behavior (see Appendix E.4.3), in realistic high-dimensional landscapes, such perfect alignment is implausible.

**Proposition 5.5** (Spectral Degeneracy,  $\gamma \rightarrow 1$ ). *Assume the per-sample Hessian spectrum is degenerate and dominated by the top  $n$  eigenvalues with approximately the same magnitude independent of  $m$ ,  $\kappa_m^{(p)} \approx \bar{\kappa}^{(p)} \gg \kappa_{\text{rest}}, (m \leq n)$ . Instead of perfect global alignment, their eigenvectors  $\mathbf{u}_m^{(p)}$  ( $m \leq n$ ) are approximately aligned across different samples  $p$  such that  $(\mathbf{u}_m^{(p)} \cdot \mathbf{v}_i)^2 \approx \delta_{mi}$  for  $i \leq n$ , while  $(\mathbf{u}_m^{(p)} \cdot \mathbf{v}_i)^2$  remains finite for  $i > n$ . Then the diagonal elements of Covariance and Hessian can be approximated as:*

$$C_{ii} \propto \mu_{\kappa^2} \sum_{m=1}^n \mathbb{E}_p[(\mathbf{u}_m^{(p)} \cdot \mathbf{v}_i)^2] = \frac{\mu_{\kappa^2}}{\mu_{\kappa}} H_{ii}, \quad (22)$$

where  $\mu_{\kappa^2} = \mathbb{E}_p[(\kappa_m^{(p)})^2]$  and  $\mu_{\kappa} = \mathbb{E}_p[\kappa_m^{(p)}]$ , implying  $\gamma \rightarrow 1$ .

We defer the proofs to Appendix E.4.

In general, the exponent  $\gamma$  captures how strongly stochastic curvature fluctuations are aligned with the global geometry of the loss landscape.

### 5.3. Distinction between CE and MSE

We now try to explain the significant difference in  $\gamma$  values between CE and MSE losses as observed in examples shown in Table 1. Empirically, we find that the per-sample hessian spectra are dominated by the first eigenvalue (i.e.,  $m = n = 1$ ), as illustrated in Figures 3 and 13 to 15 (see columns 2 and 3) for both MSE and CE losses. This empirical observation is verified by a ‘‘suppression experiment’’ as shown in (Figures 13 to 15) with details described in Appendix B.3. Briefly, to isolate the impact of the largest first eigenvalues of per-sample hessians, we suppress the

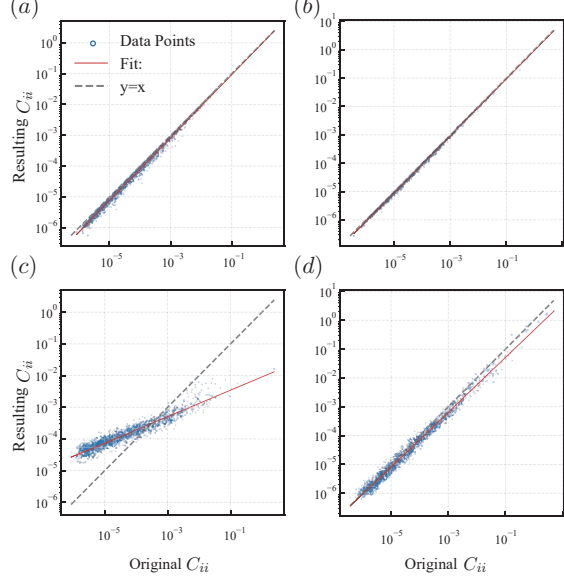


Figure 3. Log-log plots of the diagonal elements of the resulting Covariance by ‘‘suppression experiment’’ versus the original Covariance. (a, b) Covariance derived from per-sample Hessians retaining only the dominant eigenvalues. (c, d) Covariance derived after replacing the dominant eigenvalues with their mean value. Columns correspond to distinct models: (a, c) MLP on CIFAR-10 (CE loss,  $\gamma \approx 1.4$ ) and (b, d) MLP on MNIST (MSE loss,  $\gamma \approx 1$ ).

magnitude of the rest of the eigenvalues by several orders of magnitude. We find that the global Hessian spectrum  $H_{ii}$  and Covariance diagonal  $C_{ii}$  from the resulting suppressed per-sample hessians hardly change for both CE and MSE losses, as shown in Figure 3 (a,b).

The dominance of the first eigenvalue leads to a simple formula for  $C_{ii} \propto \mathbb{E}_p[(\kappa_1^{(p)})^2 (\mathbf{u}_1^{(p)} \cdot \mathbf{v}_i)^2] = \mathbb{E}_p[XY]$  expressed as the correlation between two stochastic variables of the system:  $X \equiv (\kappa_1^{(p)})^2$  – the magnitude of the first eigenvalue and  $Y \equiv (\mathbf{u}_1^{(p)} \cdot \mathbf{v}_i)^2$  – the alignment of the corresponding eigenvector with the eigenvector of  $\mathbf{H}$ . When  $X$  and  $Y$  are independent of each other, we have  $C_{ii} = \mathbb{E}_p[X] \mathbb{E}_p[Y] \propto H_{ii}$ , which means  $\gamma = 1$ . If there is a positive correlation between  $X$  and  $Y$ , it can lead to a superlinear dependence with  $\gamma > 1$ .

We posit this  $X - Y$  correlation depends on the geometry of loss function, thereby driving the distinction between CE with  $\gamma > 1$  and MSE with  $\gamma \rightarrow 1$ . To test this hypothesis, we replaced these first eigenvalues with their mean value and found that the resulting  $H_{ii}$  and  $C_{ii}$  hardly change for models with MSE loss (Figure 3 (d)) but undergo significant distortion for CE loss, especially for the case  $\gamma \sim 1.4$  (Figure 3 (c)), which leads to lowering of the exponent  $\gamma \rightarrow 1$ . We emphasize that while our experiments isolate this correlation as the reason for the distinction between MSE and CE losses, the underlying theoretical mechanism driving this

behavior remains open for future work (Soudry et al., 2018; Lu & Steinerberger, 2021).

## 6. Conclusion and Discussion

In this paper, we revisit the relationship between the covariance of SGD noise and the Hessian. By abandoning the flawed realizability assumption underlying the Fisher approximation and instead leveraging Activity-Weight Duality, we show that the noise covariance  $\mathbf{C}$  is fundamentally governed by the second moment of per-sample Hessians. This leads to a superlinear relation  $C_{ii} \propto H_{ii}^\gamma$  with  $1 \leq \gamma \leq 2$ . Crucially, the Fisher approximation fails to capture the empirically relevant superlinear regime, a limitation that is particularly consequential since  $\gamma > 1$  is intrinsic to the widely used cross-entropy loss. By resolving the microscopic distinction between MSE and CE and by robustly tracking noise-curvature alignment even during early training, our results provide a more faithful characterization of the positive  $\mathbf{C}$ - $\mathbf{H}$  relationship, thereby advancing the understanding of the implicit regularization induced by SGD.

In our analysis, we employ the explicit form of  $\Delta\mathbf{w}$  for a fully connected layer to derive the AWD-based covariance. While the explicit expression of  $\Delta\mathbf{w}$  may vary across architectures, the underlying AWD is model-agnostic. Moreover, as implied by Theorem 3.4, the final expression of  $C_{ii}$  depends on  $\Delta\mathbf{w}$  only through an overall prefactor,  $\mathbb{E}_\mu[(\mathbf{u}_m^{(p)})^\top \Delta\mathbf{w}_p^\mu (\Delta\mathbf{w}_p^\mu)^\top \mathbf{u}_n^{(p)}] \approx \sigma_w^2 \delta_{mn}$ , which is insensitive to detailed architectural choices. Consequently, we expect the superlinear dependence of  $C_{ii}$  on  $H_{ii}$  observed in our study to persist across other model families, including convolutional networks and Transformers.

Our approach is conceptually distinct from the Fisher approximation in that it directly probes the microscopic structure of per-sample Hessians, rather than relying on likelihood-based surrogate assumptions. Through the suppression experiment, we further trace the observed superlinear scaling ( $\gamma \sim 1.4 > 1$ ) to the entanglement between curvature eigenvalues and their projecting directions, thereby clarifying the fundamental difference between MSE and CE. While we hypothesize that this distinction is rooted in the differing convergence properties of KL divergence and quadratic loss (Soudry et al., 2018; Lu & Steinerberger, 2021), elucidating the precise mechanism and its implications for generalization remains an important direction for future work.

## Accessibility

To ensure the reproducibility of our results and facilitate further research, the code is open sourced at <https://anonymous.4open.science/r/AWCH-1A6A>.

## Impact Statement

This paper presents work whose goal is to advance the field of Machine Learning. There are many potential societal consequences of our work, none of which we feel must be specifically highlighted here.

## References

Arpit, D., Jastrzunek, S., Ballas, N., Krueger, D., Bengio, E., Kanwal, M. S., Maharaj, T., Fischer, A., Courville, A., Bengio, Y., and Lacoste-Julien, S. A closer look at memorization in deep networks. In *Proceedings of the 34th International Conference on Machine Learning - Volume 70*, ICML’17, pp. 233–242. JMLR.org, 2017.

Bottou, L. Stochastic gradient learning in neural networks. In *Proceedings of Neuro-Nîmes 91*, Nîmes, France, 1991. EC2. URL <http://leon.bottou.org/papers/bottou-91c>.

Brutzkus, A., Globerson, A., Malach, E., and Shalev-Shwartz, S. Sgd learns over-parameterized networks that provably generalize on linearly separable data, 2017. URL <https://arxiv.org/abs/1710.10174>.

Chaudhari, P. and Soatto, S. Stochastic gradient descent performs variational inference, converges to limit cycles for deep networks. *arXiv:1710.11029 [cond-mat, stat]*, January 2018.

Chaudhari, P., Choromanska, A., Soatto, S., LeCun, Y., Baldassi, C., Borgs, C., Chayes, J., Sagun, L., and Zecchina, R. Entropy-SGD: Biasing gradient descent into wide valleys. *Journal of Statistical Mechanics: Theory and Experiment*, 2019(12):124018, December 2019. ISSN 1742-5468. doi: 10.1088/1742-5468/ab39d9.

Daneshmand, H., Kohler, J., Lucchi, A., and Hofmann, T. Escaping saddles with stochastic gradients. In Dy, J. and Krause, A. (eds.), *Proceedings of the 35th International Conference on Machine Learning*, volume 80 of *Proceedings of Machine Learning Research*, pp. 1155–1164. PMLR, 10–15 Jul 2018. URL <https://proceedings.mlr.press/v80/daneshmand18a.html>.

Dauphin, Y., Pascanu, R., Gulcehre, C., Cho, K., Ganguli, S., and Bengio, Y. Identifying and attacking the saddle point problem in high-dimensional non-convex optimization. *arXiv:1406.2572 [cs, math, stat]*, June 2014.

Dinh, L., Pascanu, R., Bengio, S., and Bengio, Y. Sharp minima can generalize for deep nets. In Precup, D. and Teh, Y. W. (eds.), *Proceedings of the 34th International Conference on Machine Learning*, volume 70 of *Proceedings of*

*Machine Learning Research*, pp. 1019–1028. PMLR, 06–11 Aug 2017. URL <https://proceedings.mlr.press/v70/dinh17b.html>.

Dziugaite, G. K. and Roy, D. M. Computing nonvacuous generalization bounds for deep (stochastic) neural networks with many more parameters than training data. *CoRR*, abs/1703.11008, 2017. URL <https://arxiv.org/abs/1703.11008>.

Feng, Y. and Tu, Y. The inverse variance–flatness relation in stochastic gradient descent is critical for finding flat minima. *Proceedings of the National Academy of Sciences*, 118(9):e2015617118, March 2021. ISSN 0027-8424, 1091–6490. doi: 10.1073/pnas.2015617118.

Feng, Y., Zhang, W., and Tu, Y. Activity–weight duality in feed-forward neural networks reveals two co-determinants for generalization. *Nature Machine Intelligence*, 5(8):908–918, August 2023. ISSN 2522-5839. doi: 10.1038/s42256-023-00700-x.

Ghorbani, B., Krishnan, S., and Xiao, Y. An investigation into neural net optimization via hessian eigenvalue density. In *ICML*, volume 97 of *Proceedings of Machine Learning Research*, pp. 2232–2241. PMLR, 2019.

HaoChen, J. Z., Wei, C., Lee, J., and Ma, T. Shape Matters: Understanding the Implicit Bias of the Noise Covariance. In *Proceedings of Thirty Fourth Conference on Learning Theory*, pp. 2315–2357. PMLR, July 2021.

Hardt, M., Recht, B., and Singer, Y. Train faster, generalize better: Stability of stochastic gradient descent. In Balcan, M. F. and Weinberger, K. Q. (eds.), *Proceedings of The 33rd International Conference on Machine Learning*, volume 48 of *Proceedings of Machine Learning Research*, pp. 1225–1234, New York, New York, USA, 20–22 Jun 2016. PMLR. URL <https://proceedings.mlr.press/v48/hardt16.html>.

Hochreiter, S. and Schmidhuber, J. Flat minima. *Neural Computation*, 9(1):1–42, 1997. doi: 10.1162/NECO.1997.9.1.1.

Hoffer, E., Hubara, I., and Soudry, D. Train longer, generalize better: Closing the generalization gap in large batch training of neural networks. In *Advances in Neural Information Processing Systems*, volume 30. Curran Associates, Inc., 2017.

Hu, W., Li, C. J., Li, L., and Liu, J.-G. On the diffusion approximation of nonconvex stochastic gradient descent, 2018. URL <https://arxiv.org/abs/1705.07562>.

Jacot, A., Gabriel, F., and Hongler, C. The asymptotic spectrum of the hessian of dnn throughout training. In *International Conference on Learning Representations*, 2020. URL <https://openreview.net/forum?id=SkgscaNYPS>.

Jastrzebski, S., Kenton, Z., Arpit, D., Ballas, N., Fischer, A., Bengio, Y., and Storkey, A. Three factors influencing minima in SGD. In *International Conference on Artificial Neural Networks (ICANN)*, pp. 169–180. Springer, 2018.

Jiang, Y., Neyshabur, B., Mobahi, H., Krishnan, D., and Bengio, S. Fantastic Generalization Measures and Where to Find Them. In *International Conference on Learning Representations*, March 2020.

Jin, C., Ge, R., Netrapalli, P., Kakade, S. M., and Jordan, M. I. How to escape saddle points efficiently. In Precup, D. and Teh, Y. W. (eds.), *Proceedings of the 34th International Conference on Machine Learning*, volume 70 of *Proceedings of Machine Learning Research*, pp. 1724–1732. PMLR, 06–11 Aug 2017. URL <https://proceedings.mlr.press/v70/jin17a.html>.

Kaur, S., Cohen, J., and Lipton, Z. C. On the Maximum Hessian Eigenvalue and Generalization. In *Proceedings On*, pp. 51–65. PMLR, February 2023.

Keskar, N. S., Mudigere, D., Nocedal, J., Smelyanskiy, M., and Tang, P. T. P. On large-batch training for deep learning: Generalization gap and sharp minima. In *ICLR*, 2017.

Krizhevsky, A., Hinton, G., et al. Learning multiple layers of features from tiny images. Technical Report TR-2009, University of Toronto, Toronto, Ontario, 2009.

LeCun, Y. The mnist database of handwritten digits. <http://yann.lecun.com/exdb/mnist/>, 1998.

LeCun, Y., Bengio, Y., and Hinton, G. Deep learning. *Nature*, 521(7553):436–444, 2015. ISSN 1476-4687. doi: 10.1038/nature14539. URL <https://doi.org/10.1038/nature14539>.

Li, Q., Tai, C., and Weinan, E. Stochastic modified equations and adaptive stochastic gradient algorithms. In *International Conference on Machine Learning*, pp. 2101–2110. PMLR, 2017.

Li, X., Gu, Q., Zhou, Y., Chen, T., and Banerjee, A. Hessian based analysis of sgd for deep nets: Dynamics and generalization, 2019. URL <https://arxiv.org/abs/1907.10732>.

Li, Y. and Yuan, Y. Convergence analysis of two-layer neural networks with relu activation. In Guyon, I., Luxburg, 2017.

U. V., Bengio, S., Wallach, H., Fergus, R., Vishwanathan, S., and Garnett, R. (eds.), *Advances in Neural Information Processing Systems*, volume 30. Curran Associates, Inc., 2017. URL [https://proceedings.neurips.cc/paper\\_files/paper/2017/file/a96b65a721e561e1e3de768ac819ffbb-Paper.pdf](https://proceedings.neurips.cc/paper_files/paper/2017/file/a96b65a721e561e1e3de768ac819ffbb-Paper.pdf).

Li, Z., Malladi, S., and Arora, S. On the validity of modeling sgd with stochastic differential equations (sdes), 2021. URL <https://arxiv.org/abs/2102.12470>.

Liu, C., Zhu, L., and Belkin, M. Loss landscapes and optimization in over-parameterized non-linear systems and neural networks. *Applied and Computational Harmonic Analysis*, 59:85–116, July 2022. ISSN 10635203. doi: 10.1016/j.acha.2021.12.009.

Liu, S., Papailiopoulos, D., and Achlioptas, D. Bad Global Minima Exist and SGD Can Reach Them. In *Advances in Neural Information Processing Systems*, volume 33, pp. 8543–8552. Curran Associates, Inc., 2020.

Lu, J. and Steinerberger, S. Neural collapse with cross-entropy loss, 2021. URL <https://arxiv.org/abs/2012.08465>.

Mandt, S., Hoffman, M. D., and Blei, D. M. Stochastic gradient descent as approximate bayesian inference. *Journal of Machine Learning Research*, 18(134):1–35, 2017. URL <http://jmlr.org/papers/v18/17-214.html>.

Meurant, G. and Strakoš, Z. The lanczos and conjugate gradient algorithms in finite precision arithmetic. *Acta Numerica*, 15:471–542, 2006. doi: 10.1017/S096249290626001X.

Neelakantan, A., Vilnis, L., Le, Q. V., Sutskever, I., Kaiser, L., Kurach, K., and Martens, J. Adding gradient noise improves learning for very deep networks. *ArXiv*, abs/1511.06807, 2015. URL <https://api.semanticscholar.org/CorpusID:826188>.

Neyshabur, B., Bhojanapalli, S., McAllester, D., and Srebro, N. Exploring generalization in deep learning. In *Proceedings of the 31st International Conference on Neural Information Processing Systems*, NIPS’17, pp. 5949–5958, Red Hook, NY, USA, 2017. Curran Associates Inc. ISBN 9781510860964.

Nguyen, T. H., Simsekli, U., Gurbuzbalaban, M., and RICHARD, G. First Exit Time Analysis of Stochastic Gradient Descent Under Heavy-Tailed Gradient Noise. In *Advances in Neural Information Processing Systems*, volume 32. Curran Associates, Inc., 2019.

Papyan, V. Measurements of three-level hierarchical structure in the outliers in the spectrum of deepnet hessians, 2019a. URL <https://arxiv.org/abs/1901.08244>.

Papyan, V. The Full Spectrum of Deepnet Hessians at Scale: Dynamics with SGD Training and Sample Size, June 2019b.

Raginsky, M., Rakhlin, A., and Telgarsky, M. Non-convex learning via stochastic gradient langevin dynamics: a nonasymptotic analysis. In Kale, S. and Shamir, O. (eds.), *Proceedings of the 2017 Conference on Learning Theory*, volume 65 of *Proceedings of Machine Learning Research*, pp. 1674–1703. PMLR, 07–10 Jul 2017. URL <https://proceedings.mlr.press/v65/raginsky17a.html>.

Robbins, H. and Monro, S. A Stochastic Approximation Method. *The Annals of Mathematical Statistics*, 22(3):400–407, 1951. ISSN 0003-4851.

Sagun, L., Bottou, L., and LeCun, Y. Eigenvalues of the Hessian in Deep Learning: Singularity and Beyond, October 2017.

Sagun, L., Evci, U., Guney, V. U., Dauphin, Y., and Bottou, L. Empirical Analysis of the Hessian of Over-Parametrized Neural Networks. *arXiv:1706.04454 [cs]*, May 2018.

Sato, I. and Nakagawa, H. Approximation analysis of stochastic gradient langevin dynamics by using fokker-planck equation and ito process. In Xing, E. P. and Jebara, T. (eds.), *Proceedings of the 31st International Conference on Machine Learning*, volume 32 of *Proceedings of Machine Learning Research*, pp. 982–990, Beijing, China, 22–24 Jun 2014. PMLR. URL <https://proceedings.mlr.press/v32/satoa14.html>.

Smith, S. L. and Le, Q. V. A Bayesian Perspective on Generalization and Stochastic Gradient Descent, February 2018.

Soudry, D., Hoffer, E., and Srebro, N. The implicit bias of gradient descent on separable data. In *International Conference on Learning Representations*, 2018. URL <https://openreview.net/forum?id=r1q7n9gAb>.

Sun, R., Li, D., Liang, S., Ding, T., and Srikant, R. The Global Landscape of Neural Networks: An Overview. *IEEE Signal Processing Magazine*, 37(5):95–108, September 2020. ISSN 1053-5888, 1558-0792. doi: 10.1109/MSP.2020.3004124.

Tang, Q.-Y., Gu, Y., Cai, Y., Sun, M., Li, P., Zhou Xun, and Xie, Z. Investigating the overlooked hessian structure: From CNNs to LLMs. In *Forty-second International Conference on Machine Learning*, 2025. URL <https://openreview.net/forum?id=o62ZzfCEwZ>.

Tsuzuku, Y., Sato, I., and Sugiyama, M. Normalized flat minima: Exploring scale invariant definition of flat minima for neural networks using PAC-Bayesian analysis. In III, H. D. and Singh, A. (eds.), *Proceedings of the 37th International Conference on Machine Learning*, volume 119 of *Proceedings of Machine Learning Research*, pp. 9636–9647. PMLR, 13–18 Jul 2020. URL <https://proceedings.mlr.press/v119/tsuzuku20a.html>.

Wu, L., Zhu, Z., and E, W. Towards Understanding Generalization of Deep Learning: Perspective of Loss Landscapes. *arXiv:1706.10239 [cs, stat]*, November 2017.

Wu, L., Ma, C., and E, W. How SGD selects the global minima in over-parameterized learning: A dynamical stability perspective. In *NeurIPS*, pp. 8289–8298, 2018.

Xie, Z., He, F., Fu, S., Sato, I., Tao, D., and Sugiyama, M. Artificial Neural Variability for Deep Learning: On Overfitting, Noise Memorization, and Catastrophic Forgetting. *Neural Computation*, 33(8):2163–2192, July 2021a. ISSN 0899-7667, 1530-888X. doi: 10.1162/neco\_a\_01403.

Xie, Z., Sato, I., and Sugiyama, M. A diffusion theory for deep learning dynamics: Stochastic gradient descent exponentially favors flat minima. In *ICLR*, 2021b.

Xie, Z., Tang, Q.-Y., Sun, M., and Li, P. On the overlooked structure of stochastic gradients. In *NeurIPS*, 2023.

Xing, C., Arpit, D., Tsirigotis, C., and Bengio, Y. A Walk with SGD, May 2018.

Xu, P., Chen, J., Zou, D., and Gu, Q. Global convergence of langevin dynamics based algorithms for nonconvex optimization. In Bengio, S., Wallach, H., Larochelle, H., Grauman, K., Cesa-Bianchi, N., and Garnett, R. (eds.), *Advances in Neural Information Processing Systems*, volume 31. Curran Associates, Inc., 2018. URL [https://proceedings.neurips.cc/paper\\_files/paper/2018/file/9c19a2a1d84e04b0bd4bc888792bd1e-Paper.pdf](https://proceedings.neurips.cc/paper_files/paper/2018/file/9c19a2a1d84e04b0bd4bc888792bd1e-Paper.pdf).

Yang, N., Tang, C., and Tu, Y. Stochastic Gradient Descent Introduces an Effective Landscape-Dependent Regularization Favoring Flat Solutions. *Physical Review Letters*, 130(23):237101, June 2023. ISSN 0031-9007, 1079-7114. doi: 10.1103/PhysRevLett.130.237101.

Yang, N., Zhang, Y., Ouyang, Q., Tang, C., and Tu, Y. Transient learning dynamics drive escape from sharp valleys in stochastic gradient descent, 2026. URL <https://arxiv.org/abs/2601.10962>.

Yao, Z., Gholami, A., Lei, Q., Keutzer, K., and Mahoney, M. W. Hessian-based analysis of large batch training and robustness to adversaries. In Bengio, S., Wallach, H., Larochelle, H., Grauman, K., Cesa-Bianchi, N., and Garnett, R. (eds.), *Advances in Neural Information Processing Systems*, volume 31. Curran Associates, Inc., 2018. URL [https://proceedings.neurips.cc/paper\\_files/paper/2018/file/102f0bb6efb3a6128a3c750dd16729be-Paper.pdf](https://proceedings.neurips.cc/paper_files/paper/2018/file/102f0bb6efb3a6128a3c750dd16729be-Paper.pdf).

Yao, Z., Gholami, A., Keutzer, K., and Mahoney, M. W. Pyhessian: Neural networks through the lens of the hessian. *CoRR*, abs/1912.07145, 2019. URL <https://arxiv.org/abs/1912.07145>.

Zhang, C., Bengio, S., Hardt, M., Recht, B., and Vinyals, O. Understanding deep learning requires rethinking generalization. *arXiv:1611.03530 [cs]*, February 2017.

Zhang, Y., Liang, P., and Charikar, M. A hitting time analysis of stochastic gradient langevin dynamics, 2018. URL <https://arxiv.org/abs/1702.05575>.

Zhang, Y., Li, Y., Zhang, Z., Null, T. L., and Xu, Z.-Q. J. Embedding Principle: A Hierarchical Structure of Loss Landscape of Deep Neural Networks. *Journal of Machine Learning*, 1(1):60–113, June 2022. ISSN 2790-203X, 2790-2048. doi: 10.4208/jml.220108.

Zhou, M., Liu, T., Li, Y., Lin, D., Zhou, E., and Zhao, T. Toward understanding the importance of noise in training neural networks. In Chaudhuri, K. and Salakhutdinov, R. (eds.), *Proceedings of the 36th International Conference on Machine Learning*, volume 97 of *Proceedings of Machine Learning Research*, pp. 7594–7602. PMLR, 09–15 Jun 2019. URL <https://proceedings.mlr.press/v97/zhou19d.html>.

Zhu, Z., Wu, J., Yu, B., Wu, L., and Ma, J. The anisotropic noise in stochastic gradient descent: Its behavior of escaping from sharp minima and regularization effects. In *ICML*, volume 97 of *Proceedings of Machine Learning Research*, pp. 7654–7663. PMLR, 2019.

## A. Related Works

**Flat Minima and Generalization.** It is widely accepted that SGD tend to converge to flat minima closely related with good generalization, despite the non-convex loss landscape (Hochreiter & Schmidhuber, 1997; Hardt et al., 2016; Keskar et al., 2017; Zhang et al., 2017; Arpit et al., 2017; Hoffer et al., 2017; Neyshabur et al., 2017; Yao et al., 2018). Specifically, flatness has been shown to be a reliable predictor of generalization (Jiang et al., 2020), with low-complexity solutions often exhibiting small Hessian norms (Wu et al., 2017). While the definition of flatness is debated due to its sensitivity to parameter rescaling (Dinh et al., 2017), recent approaches effectively address this via scale-invariant measures or PAC-Bayesian frameworks (Dziugaite & Roy, 2017; Mandt et al., 2017; Chaudhari & Soatto, 2018; Smith & Le, 2018; Tsuzuku et al., 2020). Most recently, (Feng et al., 2023) reveals that two key factors, sharpness and weight norm, act together to determine generalization by using the Activity-Weight Duality relation.

**SGD Dynamics and its Diffusion Approximation.** SGD optimization behaviors have been extensively studied from various perspectives. Early works investigated the convergence of simple one-hidden-layer neural networks (Li & Yuan, 2017; Brutzkus et al., 2017), then in non-convex setting (Daneshmand et al., 2018; Jin et al., 2017; Hu et al., 2018). On the other hand, modeling SGD as a continuous-time stochastic process is a powerful theoretical tool (Jastrzebski et al., 2018; Li et al., 2017; Mandt et al., 2017; Wu et al., 2018; Xu et al., 2018; Hu et al., 2018; Nguyen et al., 2019; Zhu et al., 2019; Xie et al., 2021b; Li et al., 2021). By modeling the evolution of parameter probability densities, research on Stochastic Gradient Langevin Dynamics (SGLD) has analyzed density diffusion under injected isotropic noise (Sato & Nakagawa, 2014; Raginsky et al., 2017; Zhang et al., 2018). Meanwhile, (Jastrzebski et al., 2018) studied the minima selection probability of SGD. (Zhu et al., 2019; Xie et al., 2021b) suggests that the anisotropic diffusion inherent in SGD leads to flatter minima compared to isotropic diffusion.

**SGD Noise Relates to the Hessian.** The Hessian of the Loss Landscape is pivotal in optimization and generalization (Ghorbani et al., 2019; Li et al., 2019; Jacot et al., 2020; Yao et al., 2018; Dauphin et al., 2014; Kaur et al., 2023). It is found that the Hessian relates to the gradient covariance matrix, and are both highly anisotropic (Sagun et al., 2017; 2018; Xing et al., 2018). Assuming an equivalence between the Fisher Information Matrix and the Hessian for negative log-likelihood losses, (Jastrzebski et al., 2018; Zhu et al., 2019; Xie et al., 2021b) argued that  $\mathbf{C}$  is proportional to  $\mathbf{H}$  at the “true parameter”. Meanwhile, empirical studies consistently reveal that the Covariance and Hessian spectrum follows a “bulk-and-outlier” structure: a massive bulk of near-zero eigenvalues and a small number of large outliers (Sagun et al., 2017; 2018; Wu et al., 2017; Papyan, 2019b;a). Recent studies analyzed the heavy-tailed structure of the SGD noise covariance and the local Hessian and discovered a Power law structure(Xie et al., 2023; Tang et al., 2025).

## B. Experimental Setup

### B.1. Architecture Details

Unless otherwise noted, our mainline models were trained on the MNIST dataset (or its fixed subset) (LeCun, 1998) and the CIFAR-10 dataset (or its fixed subset) (Krizhevsky et al., 2009). We used vanilla Stochastic Gradient Descent without extra Regularization. All models were trained to convergence with 100% training accuracy for cross-entropy (CE) or  $> 95\%$  training accuracy for mean squared error (MSE) loss. To obtain stable hessian spectra, we used a *Softmax* layer before the mean squared error.

#### B.1.1. MLP

The MLP models on MNSIT dataset consist of two hidden layers of width 50 ( $784 \rightarrow 50 \rightarrow 50 \rightarrow 10$ ), employing ReLU activations without bias. We focus on the specific weight matrix connecting the two hidden layers, treating it as a flattened parameter vector of dimension  $D = 50 \times 50 = 2500$  and calculate the Covariance  $\mathbf{C}$  and the Hessian  $\mathbf{H}$  in this subspace at each checkpoint.

The MLP models on CIFAR-10 dataset consist of three hidden layers ( $3072 \rightarrow 1000 \rightarrow 50 \rightarrow 50 \rightarrow 10$ ), employing ReLU activations without bias. We focus on the specific weight matrix connecting the last two hidden layers, treating it as a flattened parameter vector of dimension  $D = 50 \times 50 = 2500$  and calculate the Covariance  $\mathbf{C}$  and the Hessian  $\mathbf{H}$  in this subspace at each checkpoint.

### B.1.2. CNN

The CNN models on MNIST and CIFAR-10 datasets share the same architecture (with adaptive input channel), of which the config is given by  $[32, M, 64, M, 128, 128, M]$ , where the number means the channel depth (with kernel size 3 and padding 1) and  $M$  represents the *Max pooling* (with kernel size 2 and stride 2), followed by the adaptive average pooling with output dimension  $128 \times 1 \times 1$ . These feature maps are flattened into a vector of dimension 128 and fed into a classifier consisting of a hidden fully connected layer and an output layer ( $128 \rightarrow 20 \rightarrow 10$ ). We use the ReLU activation without bias. To isolate the noise from mini batch sampling, we do not use the Batch Normalization. We focus on the specific weight matrix connecting the features and the hidden layer, treating it as a flattened parameter vector of dimension  $D = 128 \times 20 = 2560$  and calculate the Covariance  $\mathbf{C}$  and the Hessian  $\mathbf{H}$  in this subspace at each checkpoint.

## B.2. Visualizations Details

In this section, we detail the experimental setup used to generate the presented visualizations including the figures and table.

### B.2.1. FIGURES DETAILS

Unless otherwise noted, the CNN model presented in the figures was trained on a fixed, balanced subset of the CIFAR-10 dataset. This subset comprises 2,000 examples per class, totaling 20,000 training samples. The model was trained using the Cross-Entropy loss function for 100 epochs, achieving convergence with 100% training accuracy. Optimization was performed using vanilla SGD with a batch size of  $B = 128$  and a learning rate of  $\eta = 0.1$ .

The MLP models presented in the figures were trained on a fixed, balanced subset of the MNIST dataset, consisting of 2,000 examples per class for a total of 20,000 training samples. Models were trained for 100 epochs using vanilla SGD with a batch size of  $B = 50$  and a learning rate of  $\eta = 0.1$ . Under these settings, model minimized with Cross-Entropy (CE) loss converged to 100% training accuracy, while that minimizing Mean Squared Error (MSE) loss achieved  $> 95\%$  training accuracy.

### B.2.2. TABLE DETAILS

Detailed training hyperparameters for the results in Table 1 are provided below. All models were optimized using vanilla SGD with a learning rate of  $\eta = 0.1$ . For each hyperparameter configuration, we performed 4 independent runs with distinct random seeds. We computed  $\gamma$  after a fixed number of training epochs. The number of top eigenvalues ( $\mathcal{N}$ ) selected for computation varied based on the number of classes  $\mathcal{C} \in \{3, 6, 10\}$  included in the training subset. In Table 3, we show the  $\gamma'_{\text{AWD}}$  (via Eq. 58), which explicitly accounts for the gradient term  $\mathbf{C}^{hg}$  and  $\mathbf{C}^{gg}$ , a slightly better approximation of  $\gamma_{\text{emp}}$ .

Table 2. Hyperparameters for models presented in Table 1.  $N_{\text{data}}$  denotes total samples per class.

MODEL	LOSS	TRAINING SETUP			EIGENVALUES ( $\mathcal{N}$ )		
		$N_{\text{data}}$	BATCH ( $B$ )	EPOCHS	$\mathcal{C} = 3$	$\mathcal{C} = 6$	$\mathcal{C} = 10$
<b>MNIST</b>							
MLP	CE	2,000	50	100	300	1,000	1,000
MLP	MSE	2,000	50	100	300	1,000	1,000
CNN	CE	2,000	50	100	200	500	1,000
CNN	MSE	5,000	128	100	200	300	800
<b>CIFAR-10</b>							
MLP	CE	2,000	100	150	800	1,500	1,500
MLP	MSE	5,000	100	100	500	1,000	1,000
CNN	CE	2,000*	128	100	500	1,000	1,500
CNN	MSE	5,000	128	500	500	500	1,000

\*For the 3-class case,  $N_{\text{data}} = 5,000$ .

## B.3. Ablation Experiments Details

In this section, we provide the precise algorithmic details for the “suppression experiment” ablation study presented in Section 5.2.

**Table 3. Verification of Activity-Weight Duality (AWD) across architectures and complexities near the global minimum for MSE loss.** The comparison covers different model architectures (MLP, CNN), datasets, and task complexities (number of classes  $\mathcal{C}$ ). For each hyperparameter configuration, we repeated the experiment 4 times and report the mean and standard deviation.

Data	Model	$\mathcal{C}$	MSE		
			$\gamma_{\text{emp}}$	$\gamma_{\text{AWD}}$	$\gamma'_{\text{AWD}}$
MNIST	MLP	3	$1.07 \pm 0.02$	$1.14 \pm 0.02$	$1.07 \pm 0.02$
		6	$1.01 \pm 0.01$	$1.08 \pm 0.01$	$1.03 \pm 0.01$
		10	$0.96 \pm 0.01$	$1.03 \pm 0.01$	$1.00 \pm 0.01$
	CNN	3	$0.99 \pm 0.01$	$1.05 \pm 0.02$	$1.02 \pm 0.02$
		6	$1.03 \pm 0.01$	$1.06 \pm 0.01$	$1.05 \pm 0.01$
		10	$0.98 \pm 0.01$	$1.05 \pm 0.01$	$1.03 \pm 0.01$
CIFAR-10	MLP	3	$1.12 \pm 0.04$	$1.17 \pm 0.03$	$1.09 \pm 0.03$
		6	$1.03 \pm 0.01$	$1.08 \pm 0.02$	$1.06 \pm 0.02$
		10	$1.00 \pm 0.02$	$1.03 \pm 0.02$	$1.03 \pm 0.02$
	CNN	3	$1.04 \pm 0.04$	$1.09 \pm 0.03$	$1.06 \pm 0.03$
		6	$1.00 \pm 0.01$	$1.01 \pm 0.01$	$0.97 \pm 0.01$
		10	$1.01 \pm 0.01$	$1.02 \pm 0.01$	$0.97 \pm 0.01$

### B.3.1. EXPERIMENTAL PROCEDURE

The procedure consists of three stages: per-sample spectral decomposition, intervention (filtering and homogenization), and global reconstruction.

**1. Per-Sample Decomposition.** For a given mini-batch of size  $B$ , we compute the per-sample Hessian  $\mathbf{h}_p$  for each sample  $p \in \{1, \dots, B\}$ . We perform a full eigen-decomposition for each sample:

$$\mathbf{h}_p = \sum_{m=1}^D \kappa_m^{(p)} \mathbf{u}_m^{(p)} (\mathbf{u}_m^{(p)})^\top, \quad (23)$$

where eigenvalues are sorted in descending order  $\kappa_1^{(p)} \geq \kappa_2^{(p)} \geq \dots$ . Since the Hessian spectrum is heavily dominated by the top mode, we focus our intervention on the principal eigenvalue  $\kappa_1^{(p)}$ .

**2. Identification of Stiff Samples.** We set a relative threshold  $\tau$  based on a percentage  $\theta$  (e.g., 10%) of the maximum principal eigenvalue observed in the batch:

$$\tau = \theta \cdot \max_{p \in \{1, \dots, B\}} \kappa_1^{(p)}. \quad (24)$$

The set of stiff samples is defined as  $\mathcal{S}_{\text{stiff}} = \{p \mid \kappa_1^{(p)} > \tau\}$ .

**3. Homogenization and Suppression.** We construct a modified curvature profile  $\tilde{\kappa}_m^{(p)}$  for each sample:

- **Stiff Sample Homogenization:** For stiff samples ( $p \in \mathcal{S}_{\text{stiff}}$ ), we replace their dominant eigenvalue  $\kappa_1^{(p)}$  with the group mean  $\bar{\kappa}_{\text{stiff}}$  to remove magnitude variance. To ensure rank-1 dominance, we suppress their tail modes ( $m > 1$ ) by a factor of  $\epsilon_{\text{tail}} = 10^{-5}$ .

$$\bar{\kappa}_{\text{stiff}} = \frac{1}{|\mathcal{S}_{\text{stiff}}|} \sum_{p \in \mathcal{S}_{\text{stiff}}} \kappa_1^{(p)}. \quad (25)$$

- **Background Suppression:** For non-stiff samples ( $p \notin \mathcal{S}_{\text{stiff}}$ ), we suppress their rank-1 still modes by a factor of  $\epsilon_{\text{bg}} = 10^{-3}$  and their tail modes ( $m > 1$ ) by a factor of  $\epsilon_{\text{tail}} = 10^{-5}$ , treating them as background noise relative to the stiff samples.

Formally, the intervened eigenvalues  $\tilde{\kappa}_m^{(p)}$  are set as:

$$\tilde{\kappa}_m^{(p)} = \begin{cases} \bar{\kappa}_{\text{stiff}} & \text{if } p \in \mathcal{S}_{\text{stiff}} \text{ and } m = 1, \\ 10^{-5} \cdot \kappa_m^{(p)} & \text{if } m > 1, \\ 10^{-3} \cdot \kappa_m^{(p)} & \text{if } p \notin \mathcal{S}_{\text{stiff}} \text{ and } m = 1 \end{cases} \quad (26)$$

**4. Global Reconstruction.** Finally, we reconstruct the global Hessian  $\tilde{\mathbf{H}}$  using the modified spectral components:

$$\tilde{H}_{ii} = \frac{1}{B} \sum_{p=1}^B \sum_{m=1}^D \tilde{\kappa}_m^{(p)} \left( \mathbf{u}_m^{(p)} \cdot \mathbf{v}_i \right)^2. \quad (27)$$

We then compute the eigenvalues of this reconstructed global matrix  $\tilde{\mathbf{H}}$  and compare its spectrum to the original  $\mathbf{H}$ . We also reconstruct the covariance  $2\tilde{C}_{ii}/\sigma_w^2 = \frac{1}{B} \sum_{p=1}^B \sum_{m=1}^D (\tilde{\kappa}_m^{(p)})^2 \left( \mathbf{u}_m^{(p)} \cdot \mathbf{v}_i \right)^2$  similarly.

## C. Derivation of the Random Baseline for Scale-Invariant Alignment

In this section, we derive the theoretical expected value of the scale-invariant off-diagonal coupling under the null hypothesis of a random basis. This serves as a baseline to evaluate the statistical significance of the observed alignment between the noise covariance matrix  $\mathbf{C}$  and the Hessian  $\mathbf{H}$ .

### C.1. Problem Setup

Let  $\mathbf{C} \in \mathbb{R}^{D \times D}$  be a covariance matrix. We analyze its structure in a specific basis (e.g., the Hessian eigenbasis). The scale-invariant correlation matrix  $\mathbf{R}$  is defined as:

$$R_{ij} = \frac{C_{ij}}{\sqrt{|C_{ii}C_{jj}|}}. \quad (28)$$

We define the *mean off-diagonal coupling* metric as  $\mu_{\text{coupling}} = \mathbb{E}[|R_{ij}|]$  for  $i \neq j$ .

To establish a random baseline, we assume the **Null Hypothesis ( $H_0$ )**: The eigenvectors of  $\mathbf{C}$  are random and uniformly distributed on the orthogonal group  $O(D)$  (Haar measure), having no structural alignment with the basis of observation.

### C.2. The Spiked Spectrum Model

Deep learning optimization landscapes often exhibit a “heavy-tailed” or “spiked” spectrum. We model the spectrum of  $\mathbf{C}$  using a simplified *Spiked Covariance Model*:

- **Dominant Subspace:** The top  $M$  eigenvalues ( $\lambda_i \equiv H_{ii}$ ) contain the majority of the energy:  $\lambda_1 \approx \dots \approx \lambda_M \approx \sigma^2$ .
- **Bulk/Tail:** The remaining  $D - M$  eigenvalues are negligible:  $\lambda_{M+1} \approx \dots \approx \lambda_D \approx 0$ .
- **Sparsity:**  $M \ll D$ .

Under the random basis assumption,  $\mathbf{C}$  can be expressed as:

$$\mathbf{C} = \mathbf{Q} \Lambda \mathbf{Q}^\top, \quad (29)$$

where  $\Lambda = \text{diag}(\lambda_k)$  and  $\mathbf{Q}$  is a random orthogonal matrix. The elements of  $\mathbf{C}$  are given by:

$$C_{ij} = \sum_{k=1}^D \lambda_k Q_{ik} Q_{jk} \approx \sigma^2 \sum_{k=1}^M Q_{ik} Q_{jk}. \quad (30)$$

### C.3. Statistical Approximations in High Dimensions

For large  $D$ , the entries of a random orthogonal matrix  $\mathbf{Q}$  can be approximated as independent Gaussian variables:

$$Q_{ik} \sim \mathcal{N} \left( 0, \frac{1}{D} \right). \quad (31)$$

By using the approximation  $\mathbb{E}[|C_{ij}|/\sqrt{C_{ii}C_{jj}}] \approx \mathbb{E}[|C_{ij}|]/\mathbb{E}[\sqrt{C_{ii}C_{jj}}]$ , justified by the concentration of measure phenomenon in high-dimensional spaces. The denominator, representing the diagonal energy, is a sum of  $M$  independent squared variables, which concentrates sharply around its mean. Thus, it can be treated as a constant scalar relative to the zero-mean fluctuations of the numerator.

We now analyze the numerator and denominator of  $|R_{ij}|$  separately.

**1. The Denominator (Diagonal Elements).** The diagonal elements represent the energy projected onto each dimension:

$$C_{ii} \approx \sigma^2 \sum_{k=1}^M Q_{ik}^2. \quad (32)$$

Since  $Q_{ik}^2$  follows a scaled Chi-squared distribution with 1 degree of freedom, its expectation is  $\mathbb{E}[Q_{ik}^2] = \frac{1}{D}$ . By the Law of Large Numbers (since  $M$  is sufficiently large but  $M \ll D$ ), the sum concentrates around its mean:

$$C_{ii} \approx \mathbb{E}[C_{ii}] = \sigma^2 \cdot M \cdot \frac{1}{D} = \frac{M\sigma^2}{D}. \quad (33)$$

Thus, the normalization factor in the denominator is approximately:

$$\text{Denom} = \sqrt{C_{ii}C_{jj}} \approx \frac{M\sigma^2}{D}. \quad (34)$$

**2. The Numerator (Off-Diagonal Elements).** For  $i \neq j$ , the off-diagonal element is a sum of products:

$$C_{ij} \approx \sigma^2 \sum_{k=1}^M Q_{ik}Q_{jk}. \quad (35)$$

Let  $X_k = Q_{ik}Q_{jk}$ . Since  $Q_{ik}$  and  $Q_{jk}$  are independent (for  $i \neq j$ ),  $\mathbb{E}[X_k] = 0$ . The variance of each term is:

$$\text{Var}(X_k) = \mathbb{E}[Q_{ik}^2]\mathbb{E}[Q_{jk}^2] = \frac{1}{D} \cdot \frac{1}{D} = \frac{1}{D^2}. \quad (36)$$

By the Central Limit Theorem (CLT), the sum  $C_{ij}$  follows a Gaussian distribution:

$$C_{ij} \sim \mathcal{N}\left(0, \sigma^4 \cdot M \cdot \frac{1}{D^2}\right). \quad (37)$$

We are interested in the expected absolute value  $\mathbb{E}[|C_{ij}|]$ . For a generic Gaussian variable  $Z \sim \mathcal{N}(0, s^2)$ , the mean absolute deviation is  $\mathbb{E}[|Z|] = \sqrt{\frac{2}{\pi}}s$ . Therefore:

$$\mathbb{E}[|C_{ij}|] \approx \sqrt{\frac{2}{\pi}} \cdot \sqrt{\frac{M\sigma^4}{D^2}} = \sqrt{\frac{2}{\pi}} \frac{\sqrt{M}\sigma^2}{D}. \quad (38)$$

#### C.4. Theoretical Baseline Result

Combining the approximations for the numerator and denominator, the scaling factors  $\sigma^2$  and  $D$  cancel out, demonstrating the scale-invariant nature of the metric:

$$\begin{aligned} \mathbb{E}[|R_{ij}|] &\approx \frac{\mathbb{E}[|C_{ij}|]}{\mathbb{E}[\sqrt{C_{ii}C_{jj}}]} \\ &\approx \frac{\sqrt{\frac{2}{\pi}} \frac{\sqrt{M}\sigma^2}{D}}{\frac{M\sigma^2}{D}}. \end{aligned} \quad (39)$$

Simplifying the expression yields the final theoretical baseline:

$$\mathbb{E}[|R_{ij}|] \approx \sqrt{\frac{2}{\pi}} \frac{1}{\sqrt{M}} \approx \frac{0.8}{\sqrt{M}}. \quad (40)$$

### C.5. Interpretation

This derivation leads to two key insights:

1. **Effective Dimension Collapse:** In a spiked model, the “random noise floor” is determined not by the total dimension  $N$ , but by the effective dimension (number of spikes)  $M$ .
2. **High Background Noise:** For a typical deep learning setting where the spectrum is sharp (e.g.,  $M \approx 20 - 50$ ), the random baseline is relatively high (0.11 – 0.18).

Therefore, an observed coupling value significantly lower than  $\frac{0.8}{\sqrt{M}}$  indicates a **statistically significant structural alignment** that effectively suppresses the geometric “leakage” expected from random projections.

## D. Statistical Significance of the Alignment (P-Value Calculation)

In Appendix C, we derived the expected mean off-diagonal coupling  $\mathbb{E}[\mu_{\text{rand}}]$  under the null hypothesis of a random basis. In this section, we rigorously quantify the statistical significance of our observed results by calculating the P-value.

### D.1. Hypothesis Testing Framework

We define the null hypothesis  $H_0$  and the alternative hypothesis  $H_1$  as follows:

- $H_0$  (**Random Alignment**): The covariance matrix  $\mathbf{C}$  is structurally uncorrelated with the Hessian basis. The observed coupling  $\mu_{\text{obs}}$  is a realization from the distribution of random orthogonal projections.
- $H_1$  (**Geometric Alignment**): The covariance matrix exhibits structural alignment with the Hessian, resulting in a coupling  $\mu_{\text{obs}}$  significantly lower than expected by chance.

The test statistic is the mean off-diagonal scale-invariant coupling:

$$\bar{R} = \frac{1}{D(D-1)} \sum_{i \neq j} |R_{ij}|. \quad (41)$$

### D.2. Derivation of the Z-Score

Given the high dimensionality ( $D \approx 2000$ ), the number of off-diagonal terms  $K = D(D-1) \approx 4 \times 10^6$  is extremely large. According to the Central Limit Theorem (CLT), the sampling distribution of the mean  $\bar{R}$  under  $H_0$  converges to a Gaussian distribution:

$$\bar{R} \sim \mathcal{N}(\mu_{H_0}, \text{SE}^2). \quad (42)$$

**1. Theoretical Mean ( $\mu_{H_0}$ ).** As derived in (40), for a spectrum dominated by  $M$  effective spikes:

$$\mu_{H_0} \approx \sqrt{\frac{2}{\pi}} \frac{1}{\sqrt{M}}. \quad (43)$$

**2. Standard Error (SE).** The variance of a single absolute off-diagonal element  $|R_{ij}|$  (which follows a Folded Normal distribution derived from a variable with variance  $\tau^2 \approx 1/M$ ) is:

$$\sigma_{\text{single}}^2 = \tau^2 \left(1 - \frac{2}{\pi}\right) = \frac{1}{M} \left(1 - \frac{2}{\pi}\right). \quad (44)$$

The Standard Error of the mean over  $K \approx D^2$  terms is:

$$\text{SE} = \frac{\sigma_{\text{single}}}{\sqrt{K}} \approx \frac{1}{D} \sqrt{\frac{1}{M} \left(1 - \frac{2}{\pi}\right)}. \quad (45)$$

**3. Calculation of Z-Statistic.** The Z-score measures how many standard deviations the observed value deviates from the random baseline:

$$Z = \frac{\mu_{\text{obs}} - \mu_{H_0}}{\text{SE}}. \quad (46)$$

### D.3. Numerical Evaluation

We apply this framework to our experimental observations (CNN on CIFAR-10) with the following parameters:

- Matrix Dimension:  $D \approx 2560$ .
- Effective Spikes (estimated from spectrum):  $M \approx 20$ .
- Observed Coupling:  $\mu_{\text{obs}} \approx 0.066$ .

#### Step 1: Calculate $H_0$ Parameters.

$$\mu_{H_0} \approx 0.8 \cdot \frac{1}{\sqrt{20}} \approx 0.178. \quad (47)$$

$$\sigma_{\text{single}} \approx \sqrt{\frac{1}{20} \left(1 - \frac{2}{\pi}\right)} \approx 0.135. \quad (48)$$

$$\text{SE} \approx \frac{0.135}{2560} \approx 5.27 \times 10^{-5}. \quad (49)$$

#### Step 2: Calculate Z-Score.

$$Z = \frac{0.066 - 0.178}{5.27 \times 10^{-5}} \approx \frac{-0.128}{0.0000675} \approx -3378. \quad (50)$$

**Step 3: P-Value.** The one-sided P-value is the probability of observing a Z-score of  $-3378$  or lower under the standard normal distribution:

$$p\text{-value} = P(Z \leq -3378) \approx 0. \quad (51)$$

### D.4. Conclusion

The calculated Z-score is negative with a magnitude exceeding  $10^3$ , corresponding to a P-value that is effectively zero.

This result provides overwhelming statistical evidence to reject the null hypothesis. It confirms that the observed low coupling ( $\mu_{\text{obs}} \approx 0.066$ ) is not a statistical fluctuation or a result of the heavy-tailed spectrum, but rather a robust, deterministic geometric alignment between the SGD noise and the Hessian landscape.

## E. Proofs

### E.1. Proof of Lemma 3.2 (Feng et al., 2023)

*Proof.* The constraint  $(W + \Delta W)\mathbf{a} = W(\mathbf{a} + \Delta \mathbf{a})$  simplifies to the linear equation  $\Delta W\mathbf{a} = W\Delta \mathbf{a}$ . Since the Frobenius norm  $\|\Delta W\|_F^2 = \sum_{j=1}^{H_2} \|\Delta \mathbf{w}_j\|^2$  is separable across rows, we can solve the optimization problem independently for each row  $j$ . Let  $\Delta \mathbf{w}_j^\top$  and  $\mathbf{w}_j^\top$  denote the  $j$ -th rows of  $\Delta W$  and  $W$ , respectively. The constraint for the  $j$ -th output neuron becomes:

$$\Delta \mathbf{w}_j^\top \mathbf{a} = \mathbf{w}_j^\top \Delta \mathbf{a}. \quad (52)$$

To find the minimum norm solution for  $\Delta \mathbf{w}_j$ , we construct the Lagrangian:

$$L_j = \|\Delta \mathbf{w}_j\|^2 - \lambda_j (\Delta \mathbf{w}_j^\top \mathbf{a} - C_j), \quad (53)$$

where  $C_j = \mathbf{w}_j^\top \Delta \mathbf{a}$  is a scalar constant determined by the specific row weights and activity perturbation. Solving  $\nabla_{\Delta \mathbf{w}_j} L_j = 0$  yields  $\Delta \mathbf{w}_j = \frac{\lambda_j}{2} \mathbf{a}$ . Substituting this back into the constraint gives  $\frac{\lambda_j}{2} \|\mathbf{a}\|^2 = C_j$ , which implies  $\frac{\lambda_j}{2} = \frac{C_j}{\|\mathbf{a}\|^2}$ . Thus, the optimal row vector is:

$$\Delta \mathbf{w}_j = \frac{\mathbf{w}_j^\top \Delta \mathbf{a}}{\|\mathbf{a}\|^2} \mathbf{a}. \quad (54)$$

In element-wise notation, the  $i$ -th component of the  $j$ -th row is  $\Delta W_{ji} = \frac{a_i}{\|\mathbf{a}\|^2} \sum_k W_{jk} \Delta a_k$ . Stacking these rows back into a matrix yields the outer product form  $\Delta W = \frac{(W \Delta \mathbf{a}) \mathbf{a}^\top}{\|\mathbf{a}\|^2}$ .  $\square$

## E.2. Proof of Theorem 3.4

In this appendix, we provide the rigorous mathematical derivation of the relationship between the SGD noise covariance and the spectral properties of the per-sample Hessian. We proceed by approximating the gradient noise via Activity-Weight Duality (AWD), transforming the system into the eigenbasis of the global Hessian, and utilizing the spectral decomposition of individual samples to obtain the final result.

### E.2.1. PROOF OF LEMMA 3.3

The SGD noise covariance is defined as the expectation of the outer product of the gradient difference between mini-batches. Let  $\mathbf{g}_{\mu\nu} = \nabla \mathcal{L}^\mu(\mathbf{w}) - \nabla \mathcal{L}^\nu(\mathbf{w})$ . The covariance matrix is given by:

$$\mathbf{C} = \frac{1}{2} \mathbb{E}_{\mu, \nu} [\mathbf{g}_{\mu\nu} \mathbf{g}_{\mu\nu}^\top]. \quad (55)$$

Utilizing the Activity-Weight Duality (AWD), the loss difference arising from data sampling can be mapped to a weight perturbation  $\Delta \mathbf{w}^{\mu\nu}$ . Specifically, for a sample  $\mathbf{x}_p^\nu$  in batch  $\mathcal{B}_\nu$ , the variation is approximated by the first-order Taylor expansion in weight space:

$$\ell(\mathbf{x}_p^\nu; \mathbf{w}) - \ell(\mathbf{x}_p^\nu; \mathbf{w} + \Delta \mathbf{w}^{\mu\nu}) \approx - \sum_{i,j} \frac{\partial \ell(\mathbf{x}_p^\nu)}{\partial w_{ij}} \Delta w_{ij}^{\mu\nu}. \quad (56)$$

To find the gradient noise vector  $\mathbf{g}_{\mu\nu}$ , we differentiate this expression with respect to the weights  $w_{mn}$ . By applying the chain rule, the total variation in the gradient consists of two distinct terms:

$$(\mathbf{g}_{\mu\nu})_{mn} \approx \frac{1}{B} \left[ \underbrace{\sum_{p \in \mathcal{B}_\nu} \sum_{i,j} \frac{\partial^2 \ell(\mathbf{x}_p^\nu)}{\partial w_{mn} \partial w_{ij}} \Delta w_{ij}^{\mu\nu}}_{\text{Term I: Hessian-Weight}} + \underbrace{\sum_{p \in \mathcal{B}_\nu} \sum_{i,j} \frac{\partial \ell(\mathbf{x}_p^\nu)}{\partial w_{ij}} \frac{\partial (\Delta w_{ij}^{\mu\nu})}{\partial w_{mn}}}_{\text{Term II: Gradient-Activity}} \right]. \quad (57)$$

Substituting into Eq.55 gives the simplified expression of  $\mathbf{C}$ :

$$\mathbf{C} \approx \mathbf{C}_{\text{AWD, raw}} = \frac{1}{2B^2} \mathbb{E}_{\mu, \nu} (\text{Term I}^2 + 2 \text{Term I} \times \text{Term II} + \text{Term II}^2) \quad (58)$$

To better illustrate the numerical verification of the following approximation, we denote that  $\mathbf{C}^{hh} := \frac{1}{2B^2} \mathbb{E}_{\mu, \nu} (\text{Term I}^2)$ ,  $\mathbf{C}^{hg} := \frac{1}{2B^2} \mathbb{E}_{\mu, \nu} (\text{Term I} \times \text{Term II})$  and  $\mathbf{C}^{gg} := \frac{1}{2B^2} \mathbb{E}_{\mu, \nu} (\text{Term II} \times \text{Term II})$ . Then we have:

$$\mathbf{C} \approx \mathbf{C}_{\text{AWD, raw}} = \mathbf{C}^{hh} + \mathbf{C}^{hg} + \mathbf{C}^{gg} \quad (59)$$

### Analysis of Terms:

- **Term I (Hessian Dominance):** This term represents the interaction between the per-sample Hessian  $\mathbf{h}_p = \nabla^2 \ell(\mathbf{x}_p; \mathbf{w})$  and the AWD weight perturbation. In vector notation, this is  $\mathbf{h}_p \Delta \mathbf{w}^{\mu\nu}$ .
- **Term II (Activity Gradients):** The AWD solution is given by  $\Delta w_{ij} \propto a_i \sum_k \Delta a_k w_{kj}$ . The derivative  $\frac{\partial \Delta w}{\partial w}$  introduces terms depending on the activity perturbation  $\Delta \mathbf{a}$ . This term effectively couples the loss gradient  $\nabla \ell$  with the activity noise.

### Justification for Neglecting Term II:

The approximation in Lemma 3.3,  $\mathbf{g}_{\mu\nu} \approx \mathbf{h}_p \Delta \mathbf{w}$ , relies on the assumption that Term I dominates Term II. This is physically grounded in the dynamics of SGD near convergence:

1. **Vanishing Gradients near Global Minima:** Term II involves the gradient of the loss  $\nabla\ell$ , which acts as a scaling factor. As the model approaches a global minimum (or a high-quality local minimum), the per-sample gradients for correctly classified examples tend to vanish (i.e.,  $\|\nabla\ell\| \rightarrow 0$ ). In contrast, the Hessian  $\mathbf{h}_p$  (local curvature) remains non-zero and significant even at the minimum. Consequently, the magnitude of Term II decays significantly faster than that of Term I.
2. **Empirical Verification:** As demonstrated in our numerical experiments (referenced in Figures 4 to 6 (*f&g*)), specifically in the regime near the global minimum, the magnitude of Term I is observed to be orders of magnitude larger than that of Term II. The contribution of the gradient-activity coupling to the total noise covariance is negligible compared to the Hessian-weight coupling, which means  $\mathbf{C}^{hg}$  and  $\mathbf{C}^{gg}$  are significantly smaller than  $\mathbf{C}^{hh}$ .

Therefore, we retain only the dominant leading-order term, establishing the approximation:

$$\mathbf{g}_{\mu\nu} \approx \frac{1}{B} \sum_{p \in \mathcal{B}_\nu} \mathbf{h}_p(\mathbf{w}) \Delta \mathbf{w}_p^{\mu\nu}. \quad (60)$$

□

### E.2.2. COORDINATE TRANSFORMATION TO HESSIAN EIGENBASIS

To analyze the spectral properties of the noise, we move to the eigenbasis of the full-batch Hessian  $\mathbf{H} = \mathbb{E}_p[\mathbf{h}_p]$ . Let  $\mathbf{H} = \mathbf{V}\Lambda\mathbf{V}^\top$  be the eigendecomposition in the descending order, where  $\mathbf{V} = [\mathbf{v}_1, \dots, \mathbf{v}_D]$  is the orthogonal matrix of eigenvectors. We seek to calculate the diagonal elements of the covariance matrix in this basis, defined as  $C_{ii} = \mathbf{v}_i^\top \mathbf{C} \mathbf{v}_i$ .

### E.2.3. DETAILED PROOF OF THEOREM 3.4

*Proof.* Substituting the AWD approximation (Eq. 60) into the definition of  $C_{ii}$ , we begin with the expectation over both batches  $\mathcal{B}_\mu$  and  $\mathcal{B}_\nu$ :

$$C_{ii} \approx C_{ii}^{hh} = \frac{1}{2B^2} \mathbb{E}_{\mu, \nu} \left[ \mathbf{v}_i^\top \left( \sum_{p \in \mathcal{B}_\nu} \mathbf{h}_p \Delta \mathbf{w}_p^{\mu\nu} \right) \left( \sum_{q \in \mathcal{B}_\nu} \mathbf{h}_q \Delta \mathbf{w}_q^{\mu\nu} \right)^\top \mathbf{v}_i \right]. \quad (61)$$

Expanding the outer product into a double summation over indices  $p, q$  within batch  $\mathcal{B}_\nu$ :

$$C_{ii} \approx C_{ii}^{hh} = \frac{1}{2B^2} \mathbb{E}_\nu \left[ \sum_{p \in \mathcal{B}_\nu} \sum_{q \in \mathcal{B}_\nu} \mathbb{E}_\mu [(\mathbf{v}_i^\top \mathbf{h}_p \Delta \mathbf{w}_p^{\mu\nu}) ((\Delta \mathbf{w}_q^{\mu\nu})^\top \mathbf{h}_q \mathbf{v}_i)] \right]. \quad (62)$$

#### Step 1: Independence of Distinct Samples

We first address the cross-terms where  $p \neq q$ . The weight perturbations  $\Delta \mathbf{w}_p^{\mu\nu}$  and  $\Delta \mathbf{w}_q^{\mu\nu}$  arise from the activity differences of distinct samples relative to the random batch  $\mathcal{B}_\mu$ . Since the sampling noise is statistically independent across different examples in the high-dimensional input space, and  $\Delta \mathbf{w}$  is zero-mean relative to the batch average, the cross-correlation vanishes (as shown in Figures 4 to 6 (*h*)):

$$\mathbb{E}_\mu [\Delta \mathbf{w}_p^{\mu\nu} (\Delta \mathbf{w}_q^{\mu\nu})^\top] \approx \mathbf{0} \quad \text{for } p \neq q. \quad (63)$$

Thus, the double sum collapses to a single summation over the diagonal terms ( $p = q$ ):

$$C_{ii} \approx C_{ii}^{hh} \approx C_{ii}^{hh, SD} = \frac{1}{2B^2} \mathbb{E}_\nu \left[ \sum_{p \in \mathcal{B}_\nu} \mathbb{E}_\mu [\mathbf{v}_i^\top \mathbf{h}_p (\Delta \mathbf{w}_p^{\mu\nu} (\Delta \mathbf{w}_p^{\mu\nu})^\top) \mathbf{h}_p \mathbf{v}_i] \right]. \quad (64)$$

#### Step 2: Local Spectral Decomposition

We analyze the term  $\mathbf{h}_p(\Delta\mathbf{w}_p^{\mu\nu}(\Delta\mathbf{w}_p^{\mu\nu})^\top)\mathbf{h}_p$  by expanding it in the *local* eigenbasis of the per-sample Hessian  $\mathbf{h}_p$ . Let  $\{\kappa_m^{(p)}, \mathbf{u}_m^{(p)}\}$  denote the eigenvalue-eigenvector pairs of  $\mathbf{h}_p$ , such that  $\mathbf{h}_p = \sum_m \kappa_m^{(p)} \mathbf{u}_m^{(p)} (\mathbf{u}_m^{(p)})^\top$  and we have:

$$\mathbf{h}_p \mathbf{v}_i = \sum_m \kappa_m^{(p)} (\mathbf{u}_m^{(p)} \cdot \mathbf{v}_i) \mathbf{u}_m^{(p)}. \quad (65)$$

Substituting this expansion into the expectation term for a single sample  $p$ :

$$\begin{aligned} \mathcal{T}_p &= \mathbb{E}_\mu [(\mathbf{h}_p \mathbf{v}_i)^\top \Delta\mathbf{w}_p^{\mu\nu} (\Delta\mathbf{w}_p^{\mu\nu})^\top (\mathbf{h}_p \mathbf{v}_i)] \\ &= \sum_{m,n} \kappa_m^{(p)} \kappa_n^{(p)} (\mathbf{u}_m^{(p)} \cdot \mathbf{v}_i) (\mathbf{u}_n^{(p)} \cdot \mathbf{v}_i) \cdot \mathbb{E}_\mu [(\mathbf{u}_m^{(p)})^\top \Delta\mathbf{w}_p^{\mu\nu} (\Delta\mathbf{w}_p^{\mu\nu})^\top \mathbf{u}_n^{(p)}]. \end{aligned} \quad (66)$$

### Step 3: Isotropy in the Local Curvature Basis

The term  $\mathcal{M}_{p,mn} = \mathbb{E}_\mu [(\mathbf{u}_m^{(p)})^\top \Delta\mathbf{w}_p^{\mu\nu} (\Delta\mathbf{w}_p^{\mu\nu})^\top \mathbf{u}_n^{(p)}]$  represents the covariance of the weight perturbation projected onto the local eigen-directions  $m$  and  $n$ . Our experimental observations, shown in Figures 4 to 6 (h), indicate that the AWD-induced weight perturbations are effectively uncorrelated when projected onto the principal directions of the local curvature, leading to  $\mathcal{M}_{p,mn} \approx \sigma_w^2 \delta_{mn}$ , yielding the approximation  $C_{ii}^{hh,SD,WD}$ . Furthermore, if the variance of the weight perturbations along these directions is approximately uniform (i.e., *Local Isotropy Assumption*):

$$\mathcal{M}_{p,mn} \approx \sigma_w^2 \delta_{mn}, \quad \sigma_w^2 \text{ is independent of index } m \text{ and } p, \quad (67)$$

which can be justified by numerical results as shown in Figures 10 to 12. Applying this eliminates the cross-terms ( $m \neq n$ ) in Eq. (66), simplifying the expression to:

$$\mathcal{T}_p \approx \sigma_w^2 \sum_m (\kappa_m^{(p)})^2 (\mathbf{u}_m^{(p)} \cdot \mathbf{v}_i)^2. \quad (68)$$

### Conclusion

Substituting  $\mathcal{T}_p$  back into the batch expectation:

$$C_{ii} \approx C_{ii}^{hh} \approx C_{ii}^{hh,SD} \approx C_{ii}^{hh,SD,WD} \approx C_{ii}^{hh,SD,WD,LI} = \frac{1}{2B^2} \mathbb{E}_\nu \left[ \sum_{p \in \mathcal{B}_\nu} \sigma_w^2 \sum_m (\kappa_m^{(p)})^2 (\mathbf{u}_m^{(p)} \cdot \mathbf{v}_i)^2 \right]. \quad (69)$$

Using the linearity of expectation,  $\mathbb{E}_\nu [\sum_{p \in \mathcal{B}_\nu} (\cdot)] = B \mathbb{E}_p [(\cdot)]$ , we arrive at the final result:

$$C_{ii} \approx C_{ii}^{hh} \approx C_{ii}^{hh,SD} \approx C_{ii}^{hh,SD,WD} \approx C_{ii}^{hh,SD,WD,LI} = \frac{\sigma_w^2}{2B} \mathbb{E}_p \left[ \sum_m (\kappa_m^{(p)})^2 (\mathbf{u}_m^{(p)} \cdot \mathbf{v}_i)^2 \right]. \quad (70)$$

This confirms that the noise along a global eigen-direction  $i$  is driven by the second moment of the local curvatures  $\kappa_m^{(p)}$ , weighted by the alignment (overlap) between the local and global geometry.

Note that, since the derivation is independent of the projection to the global eigen-directions  $\mathbf{v}_i$ , we can get the expression of the off-diagonal elements  $C_{ij}$  directly by:

$$C_{ij} \approx \frac{\sigma_w^2}{2B} \mathbb{E}_p \left[ \sum_m (\kappa_m^{(p)})^2 (\mathbf{u}_m^{(p)} \cdot \mathbf{v}_i) (\mathbf{u}_m^{(p)} \cdot \mathbf{v}_j) \right]. \quad (71)$$

□

Statistically, the terms  $(\mathbf{u}_m^{(p)} \cdot \mathbf{v}_i)$  and  $(\mathbf{u}_m^{(p)} \cdot \mathbf{v}_j)$  quantify the projections of one random Vector onto two orthogonal directions  $i$  and  $j$ , thus are statistically independent with almost zero mean value, given by the extremely high dimensions  $N \sim 2000$ . Consequently, the off-diagonal elements  $C_{ij}$  vanishes as shown in Figures 7 to 9 (see the last row).

### E.3. Proof of Theorem 5.1

In this appendix, we provide the detailed proof for Theorem 5.1. We first define the necessary auxiliary variables, derive the moment inequalities, and finally show how these inequalities constrain the power-law exponent  $\gamma$ .

#### E.3.1. DEFINITIONS AND AUXILIARY VARIABLES

Consider the projection of the gradient noise and Hessian onto a specific global eigen-direction  $\mathbf{v}_i$  (the  $i$ -th eigenvector of  $H$ ). We define two auxiliary random variables,  $A_i^{(p)}$  and  $B_i^{(p)}$ , representing the first and second moments of the projected curvature for a specific sample  $p$ :

$$A_i^{(p)} := \sum_m \kappa_m^{(p)} (\mathbf{u}_m^{(p)} \cdot \mathbf{v}_i)^2, \quad B_i^{(p)} := \sum_m (\kappa_m^{(p)})^2 (\mathbf{u}_m^{(p)} \cdot \mathbf{v}_i)^2. \quad (72)$$

Here,  $\kappa_m^{(p)}$  and  $\mathbf{u}_m^{(p)}$  are the eigenvalues and eigenvectors of the per-sample Hessian  $\mathbf{h}_p$ . By definition, the global Hessian eigenvalue  $H_{ii}$  and the noise covariance diagonal  $C_{ii}$  are expectations over the dataset distribution  $\mathcal{D}$  (indexed by  $p$ ):

$$H_{ii} = \mathbb{E}_{p \sim \mathcal{D}}[A_i^{(p)}], \quad C_{ii} = \frac{\sigma_w^2}{2B} \mathbb{E}_{p \sim \mathcal{D}}[B_i^{(p)}]. \quad (73)$$

Note that for  $C_{ii}$ , we can omit the constant factor  $\sigma_w^2/2B$  for clarity as it affects the magnitude constant  $c_c$  but not the scaling exponent  $\gamma$ .

#### E.3.2. DERIVATION OF INEQUALITIES

**Proof. 1. The Lower Bound ( $H_{ii}^2 \leq \frac{2B}{\sigma_w^2} C_{ii}$ ):**

We first apply the Cauchy-Schwarz inequality to the sum defining  $A_i^{(p)}$ . Let  $x_m = \kappa_m^{(p)} (\mathbf{u}_m^{(p)} \cdot \mathbf{v}_i)$  and  $y_m = (\mathbf{u}_m^{(p)} \cdot \mathbf{v}_i)$ . Since  $\sum_m (\mathbf{u}_m^{(p)} \cdot \mathbf{v}_i)^2 = \|\mathbf{v}_i\|^2 = 1$ , the term  $A_i^{(p)}$  can be viewed as a convex combination of  $\kappa_m^{(p)}$ . Directly comparing  $A_i^{(p)}$  and  $B_i^{(p)}$ :

$$(A_i^{(p)})^2 = \left( \sum_m \kappa_m^{(p)} (\mathbf{u}_m^{(p)} \cdot \mathbf{v}_i)^2 \right)^2 \leq \left( \sum_m (\kappa_m^{(p)})^2 (\mathbf{u}_m^{(p)} \cdot \mathbf{v}_i)^2 \right) \left( \sum_m (\mathbf{u}_m^{(p)} \cdot \mathbf{v}_i)^2 \right). \quad (74)$$

Using  $\sum_m (\mathbf{u}_m^{(p)} \cdot \mathbf{v}_i)^2 = 1$ , we obtain the sample-wise inequality:

$$(A_i^{(p)})^2 \leq B_i^{(p)}. \quad (75)$$

Next, we take the expectation over samples  $p$ . Using Jensen's inequality for the convex function  $g(x) = x^2$ , we have  $(\mathbb{E}[X])^2 \leq \mathbb{E}[X^2]$ . Thus:

$$H_{ii}^2 = (\mathbb{E}_p[A_i^{(p)}])^2 \leq \mathbb{E}_p[(A_i^{(p)})^2] \leq \mathbb{E}_p[B_i^{(p)}] = \frac{2B}{\sigma_w^2} C_{ii}. \quad (76)$$

This proves the lower bound inequality.

**2. The Upper Bound ( $\frac{2B}{\sigma_w^2} C_{ii} \leq \kappa_{\max} H_{ii}$ ):**

Assume the per-sample Hessian eigenvalues are bounded by  $\kappa_{\max}$ , i.e.,  $0 \leq \kappa_m^{(p)} \leq \kappa_{\max}$  for all  $m, p$ . We can bound the second moment term  $B_i^{(p)}$ :

$$B_i^{(p)} = \sum_m \kappa_m^{(p)} \cdot \kappa_m^{(p)} (\mathbf{u}_m^{(p)} \cdot \mathbf{v}_i)^2 \leq \kappa_{\max} \sum_m \kappa_m^{(p)} (\mathbf{u}_m^{(p)} \cdot \mathbf{v}_i)^2 = \kappa_{\max} A_i^{(p)}. \quad (77)$$

Taking the expectation over  $p$  preserves the inequality:

$$\frac{2B}{\sigma_w^2} C_{ii} = \mathbb{E}_p[B_i^{(p)}] \leq \kappa_{\max} \mathbb{E}_p[A_i^{(p)}] = \kappa_{\max} H_{ii}. \quad (78)$$

This proves the upper bound inequality. Together, we get the chain of inequality:

$$\frac{\sigma_w^2}{2B} H_{ii}^2 \leq C_{ii} \leq \frac{\sigma_w^2 \kappa_{\max}}{2B} H_{ii} \quad (79)$$

E.3.3. BOUNDS ON THE SCALING EXPONENT  $\gamma$ 

We now investigate the implications of these inequalities.

Let the eigenvalues be indexed by  $i \in [1, D]$  in descending order. Given by the empirical Power-Law  $C_{ii} = c \cdot H_{ii}^\gamma$ , where  $c > 0$  is a constant. We have

$$\log C_{ii} = \gamma \log H_{ii} + \log c. \quad (80)$$

Since the logarithm is a monotonically increasing function, taking the logarithm of both sides for the two inequalities in Eq.(79) preserves the inequality, leading to:

$$\log \alpha + 2 \log H_{ii} \leq \log C_{ii} \leq \log \beta + \log H_{ii}, \quad (81)$$

where  $\alpha = \frac{\sigma_w^2}{2B} > 0$  and  $\beta = \frac{\sigma_w^2 \kappa_{\max}}{2B} > 0$ .

**Case 1: The Upper Limit ( $\gamma \leq 2$ )** Substituting Eq.(80) into the first inequality of Eq.(81) gives:

$$(2 - \gamma) \log H_{ii} \leq \log \alpha/c, \quad (82)$$

which holds for arbitrary small  $H_{ii} \ll 1$ , requiring  $\gamma \leq 2$ .

**Case 2: The Lower Limit ( $\gamma \geq 1$ )** Similarly, the second inequality of Eq.(81) leads to:

$$(\gamma - 1) \log H_{ii} \leq \log \beta/c, \quad (83)$$

which holds for arbitrary small  $H_{ii} \ll 1$ , requiring  $\gamma \geq 1$ .

Combining both cases, we conclude that the exponent is bounded by  $1 \leq \gamma \leq 2$ .  $\square$

## E.4. Proofs of Scaling Regimes

We provide the derivations for the limiting cases of the scaling exponent  $\gamma$ , utilizing the notation established in Section 5.2.

## E.4.1. PROOF OF PROPOSITION 5.3

We first define the phenomenological conditions required to observe  $\gamma = 2$ . We examine the case where the geometric alignment is perfect but the eigenvalue magnitudes are stochastic.

Assume perfect alignment between local and global basis, i.e.,  $(\mathbf{u}_m^{(p)} \cdot \mathbf{v}_i)^2 = \delta_{mi}$ , corresponding to the equality condition of the Cauchy-Schwarz inequality Eq. (74). Then the moments simplify to:

$$H_{ii} = \mathbb{E}_p[\kappa_i^{(p)}], \quad C_{ii} \propto \mathbb{E}_p[(\kappa_i^{(p)})^2]. \quad (84)$$

Using the bias-variance decomposition  $\mathbb{E}[X^2] = (\mathbb{E}[X])^2 + \text{Var}(X)$ , we write:

$$C_{ii} \propto H_{ii}^2 + \text{Var}_p(\kappa_i^{(p)}). \quad (85)$$

If  $\text{Var}_p(\kappa_i^{(p)}) \propto (\mathbb{E}_p[\kappa_i^{(p)}])^2 = H_{ii}^2$ , then:

$$C_{ii} \propto H_{ii}^2 \implies \gamma = 2. \quad (86)$$

Assume the per-sample Hessian spectrum is locally dominated by the top  $n$  eigenvalues with magnitude  $\kappa_m^{(p)} \approx \bar{\kappa}^{(p)} \gg \kappa_{\text{rest}}$ , ( $m = 1, 2, \dots, n$ ) and their associated eigenvectors are aligned (with tiny fluctuations) across different samples  $p$ . Specifically, if the curvature moment ratio is state-independent:

## E.4.2. PROOF OF PROPOSITION 5.5

**Assumptions:**

1. **Spectral Dominance:** The per-sample Hessian spectrum is locally dominated by the top  $n$  eigenvalues with magnitude  $\kappa_m^{(p)} \approx \bar{\kappa}^{(p)} \gg \kappa_{\text{rest}}$  for  $m \leq n$ .

2. **Local Alignment:** The per-sample dominant eigen-directions  $(\mathbf{u}_m^{(p)} \cdot \mathbf{v}_i)^2$  are aligned across different samples  $p$ , but with tiny fluctuation so that  $(\mathbf{u}_m^{(p)} \cdot \mathbf{v}_i)^2 \rightarrow \delta_{mi}$  for  $i \leq n$  while  $(\mathbf{u}_m^{(p)} \cdot \mathbf{v}_i)^2$  remains finite for  $i > n$ . This tiny fluctuations contribute to the bulk eigenvalues of Global Hessian which is the source of heavy-tailed spectrum.

3. **Statistical Homogeneous Magnitude:**  $\kappa_m^{(p)}$  for  $m \leq n$  are identically distributed (i.i.d.) variables drawn from a distribution characteristic of the loss basin. We define the first and second moments as characteristic constants:

$$\mathbb{E}_p[\kappa_m^{(p)}] = \mu_\kappa, \quad \mathbb{E}_p[(\kappa_m^{(p)})^2] = \mu_{\kappa^2} = \mu_\kappa^2 + \sigma_\kappa^2. \quad (87)$$

Crucially, we assume the variance  $\sigma_\kappa^2$  is an intrinsic property of the data complexity and is *independent* of the projection direction  $m$ .

**Derivation:** We evaluate the global Hessian diagonal  $H_{ii}$  and the noise covariance  $C_{ii}$  by applying the independence property  $\mathbb{E}[XY] = \mathbb{E}[X]\mathbb{E}[Y]$  under the Local Alignment assumption:

For the Hessian:

$$H_{ii} = \mathbb{E}_p \left[ \sum_{m=1}^n \kappa_m^{(p)} (\mathbf{u}_m^{(p)} \cdot \mathbf{v}_i)^2 \right] \quad (88)$$

$$= \sum_{m=1}^n \mathbb{E}_p[\kappa_m^{(p)}] \cdot \mathbb{E}_p[(\mathbf{u}_m^{(p)} \cdot \mathbf{v}_i)^2] \quad (89)$$

$$= \mu_\kappa \underbrace{\sum_{m=1}^n \mathbb{E}_p[(\mathbf{u}_m^{(p)} \cdot \mathbf{v}_i)^2]}_{\mathcal{G}_i \text{ (Geometric Factor)}}, \quad (90)$$

where the last identity results from the Statistical Homogeneous Magnitude assumption. For the Noise Covariance:

$$C_{ii} \propto \mathbb{E}_p \left[ \sum_{m=1}^n (\kappa_m^{(p)})^2 (\mathbf{u}_m^{(p)} \cdot \mathbf{v}_i)^2 \right] \quad (91)$$

$$= \sum_{m=1}^n \mathbb{E}_p[(\kappa_m^{(p)})^2] \cdot \mathbb{E}_p[(\mathbf{u}_m^{(p)} \cdot \mathbf{v}_i)^2] \quad (92)$$

$$= \mu_{\kappa^2} \sum_{m=1}^n \mathbb{E}_p[(\mathbf{u}_m^{(p)} \cdot \mathbf{v}_i)^2] \quad (93)$$

$$= \mu_{\kappa^2} \mathcal{G}_i. \quad (94)$$

**Conclusion:** Combining the two expressions, we find the relationship depends on the ratio of the moments:

$$C_{ii} \propto \frac{\mu_{\kappa^2}}{\mu_\kappa} H_{ii} = \left( \mu_\kappa + \frac{\sigma_\kappa^2}{\mu_\kappa} \right) H_{ii}. \quad (95)$$

Since  $\mu_\kappa$  and  $\sigma_\kappa^2$  are scalar constants characteristic of the dataset and do not depend on the eigen-index  $i$ , the pre-factor is a constant. Thus, the scaling relationship is approximately linear with  $\gamma \rightarrow 1$ .

#### E.4.3. DERIVATION OF THE RANDOM SHIFTS MODEL (RSM)

We define the *Random Shifts Model* where the mini-batch loss  $\mathcal{L}_\nu$  is a spatially translated version of the true population loss  $L$ :

$$\mathcal{L}_\nu(\mathbf{w}) = \mathcal{L}(\mathbf{w} - \delta\mathbf{w}^\nu), \quad (96)$$

where  $\delta\mathbf{w}^\nu \sim \mathcal{N}(0, \sigma^2 I)$  represents the effective sampling noise (shift) in the parameter space. Assuming small  $\delta\mathbf{w}^\nu$ , we perform a Taylor expansion of the gradient  $\nabla\mathcal{L}_\nu(\mathbf{w})$  around  $\mathbf{w}$ :

$$\nabla\mathcal{L}_\nu(\mathbf{w}) = \nabla\mathcal{L}(\mathbf{w} - \delta\mathbf{w}^\nu) \quad (97)$$

$$\approx \nabla\mathcal{L}(\mathbf{w}) - \nabla^2\mathcal{L}(\mathbf{w}) \cdot \delta\mathbf{w}^\nu \quad (98)$$

$$= \nabla\mathcal{L}(\mathbf{w}) - \mathbf{H}\delta\mathbf{w}^\nu. \quad (99)$$

The gradient noise vector is thus given by  $\epsilon(\mathbf{w}) = \nabla \mathcal{L}(\mathbf{w}) - \nabla \mathcal{L}_\nu(\mathbf{w}) \approx \mathbf{H} \delta \mathbf{w}^\nu$ . This explicitly demonstrates the multiplicative nature of the noise: the input perturbation  $\delta \mathbf{w}^\nu$  is amplified by the local curvature  $\mathbf{H}$ .

The noise covariance matrix  $\mathbf{C}$  is defined as the second moment of the gradient noise:

$$\mathbf{C} = \mathbb{E}_\nu[\epsilon(\mathbf{w})\epsilon(\mathbf{w})^T] \quad (100)$$

$$\approx \mathbb{E}_\nu[(\mathbf{H} \delta \mathbf{w}^\nu)(\mathbf{H} \delta \mathbf{w}^\nu)^T] \quad (101)$$

$$= \mathbf{H} \mathbb{E}_\nu[\delta \mathbf{w}^\nu \delta \mathbf{w}^{\nu T}] \mathbf{H}^T. \quad (102)$$

Substituting the isotropic noise covariance  $\mathbb{E}[\delta \mathbf{w}^\nu \delta \mathbf{w}^{\nu T}] = \sigma^2 I$ :

$$\mathbf{C} = \sigma^2 \mathbf{H}^2. \quad (103)$$

In the eigenbasis of  $\mathbf{H}$ , since  $\mathbf{H}$  and  $\mathbf{H}^2$  share the same eigenvectors, the diagonal elements satisfy  $C_{ii} \propto H_{ii}^2$ .

While this result aligns with the scaling law observed in Proposition 5.3, it remains to be figured out how the Random Shifts Model formally satisfies the *statistical variance assumption* ( $\text{Var} \sim \mathbb{E}^2$ ) used in Proposition 5.3. We establish this formal equivalence in the following section.

### Geometric Decomposition and The Alignment Assumption

To understand how the physical mechanism of random shifts (RSM) translates into the statistical observations of the Proposition 5.3, we must first analyze the geometry of Hessian perturbations.

Let  $\mathbf{H} = \mathbf{U} \Lambda \mathbf{U}^T$  be the eigendecomposition of the Hessian. Under a small random spatial shift  $\delta \mathbf{w}^\nu$ , the perturbation  $\Delta \mathbf{H} = \mathbf{H}(\mathbf{w} - \delta \mathbf{w}^\nu) - \mathbf{H}$  can be decomposed into two distinct geometric components using the product rule:

$$\Delta \mathbf{H} \approx \underbrace{\Delta \mathbf{U} \cdot \Lambda \mathbf{U}^T + \mathbf{U} \Lambda \cdot \Delta \mathbf{U}^T}_{\text{Eigenvector Rotation}} + \underbrace{\mathbf{U} \cdot \Delta \Lambda \cdot \mathbf{U}^T}_{\text{Eigenvalue Fluctuation}}. \quad (104)$$

The first term represents the rotation of the curvature axes, while the second term represents the fluctuation of the curvature magnitudes.

**The Alignment Assumption:** The Proposition 5.3 framework fundamentally assumes that noise aligns with the curvature directions (i.e.,  $(\mathbf{u}_m^{(p)} \cdot \mathbf{v}_i)^2 = \delta_{mi}$ ). Geometrically, this imposes that the Hessian variation is dominated purely by the variation of its eigenvalues:

$$\Delta \mathbf{H} \approx \mathbf{U} \Delta \Lambda \mathbf{U}^T, \quad (105)$$

which imposes a strong condition on the local geometry of the Loss Landscape that is rarely satisfied in real world, so we call this a toy model.

We can map the physical predictions of RSM onto this aligned geometric framework.

1. *The Physical Prediction (RSM):* The Random Shifts Model with isotropic sampling noise yields a noise covariance strictly quadratic in the Hessian eigenvalues:

$$C_{ii}^{\text{RSM}} = \sigma^2 (H_{ii})^2 = \sigma^2 \lambda_i^2, \quad (106)$$

where  $\lambda_i$  denotes the eigenvalues of the global Hessian.

2. *The Proposition 5.3:* Under the alignment assumption from Section E.4.1, the noise covariance is determined by the second moment of the local curvature  $\kappa_i^{(p)}$ :

$$C_{ii}^{\text{SMR}} \propto \mathbb{E}_p[(\kappa_i^{(p)})^2]. \quad (107)$$

Applying the bias-variance decomposition  $\mathbb{E}[X^2] = \text{Var}(X) + (\mathbb{E}[X])^2$  and noting that  $\mathbb{E}_p[\kappa_i^{(p)}] = \lambda_i$ , we write:

$$C_{ii}^{\text{SMR}} \propto \text{Var}_p(\kappa_i^{(p)}) + \lambda_i^2. \quad (108)$$

3. *Establishing Equivalence:* Matching the physical prediction with the statistical definition yields the constraint:

$$\sigma^2 \lambda_i^2 \propto \text{Var}_p(\kappa_i^{(p)}) + \lambda_i^2. \quad (109)$$

Rearranging terms reveals the implicit variance structure imposed by RSM:

$$\text{Var}_p(\kappa_i^{(p)}) \propto (\sigma^2 - 1)\lambda_i^2 \implies \text{Var}_p(\kappa_i^{(p)}) \propto (\mathbb{E}_p[\kappa_i^{(p)}])^2. \quad (110)$$

*Conclusion:* If the Random Shifts Model operates under strict geometric alignment, it inherently necessitates the *Statistical Variance Assumption* ( $\text{Var} \propto \mathbb{E}^2$ ).

### Micro-Geometric Origins: The Self-Similarity Condition

The derivation above establishes that for RSM to manifest as the Proposition 5.3, the variance of the eigenvalues must scale with the square of their means. We now identify the specific landscape geometry required to satisfy this condition physically.

We express the fluctuation of a specific eigenvalue  $\lambda_i$  under a spatial shift  $\delta\mathbf{w}^\nu$  using a Taylor expansion along the shift direction:

$$\lambda_i(\mathbf{w} - \delta\mathbf{w}^\nu) \approx \lambda_i(\mathbf{w}) - \nabla\lambda_i(\mathbf{w}) \cdot \delta\mathbf{w}^\nu. \quad (111)$$

Here,  $\nabla\lambda_i(\mathbf{w})$  corresponds to the diagonal element of the third-order derivative tensor  $\nabla^3\mathcal{L}$  projected onto the  $i$ -th eigenvector (denoted as  $\nabla^3\mathcal{L}_{iii}$ ). Since  $\mathbb{E}_\nu[\delta\mathbf{w}^\nu] = 0$  and  $\mathbb{E}_\nu[\delta\mathbf{w}^\nu\delta\mathbf{w}^{\nu T}] = \sigma^2 I$ , the variance of this fluctuation is:

$$\text{Var}(\lambda_i) \approx \mathbb{E}_\nu[(\nabla\lambda_i \cdot \delta\mathbf{w}^\nu)^2] = \sigma^2 \|\nabla\lambda_i\|^2. \quad (112)$$

We now invoke the statistical requirement:  $\text{Var}(\lambda_i) \propto \lambda_i^2$ . Substituting the geometric variance, we arrive at the necessary condition:

$$\sigma^2 \|\nabla\lambda_i\|^2 \propto \lambda_i^2 \implies \frac{\|\nabla\lambda_i\|}{\lambda_i} \approx \text{const.} \quad (113)$$

In tensor notation, this implies a global Self-Similarity Condition:

$$\|\nabla^3\mathcal{L}(\mathbf{w})\|^2 \propto \|\nabla^2\mathcal{L}(\mathbf{w})\|^2, \quad (114)$$

which exposes another strong condition on the local geometry of the Loss Landscape that is rarely satisfied in real world. Therefore, we conclude that the Proposition 5.3 hardly exists in Real world.

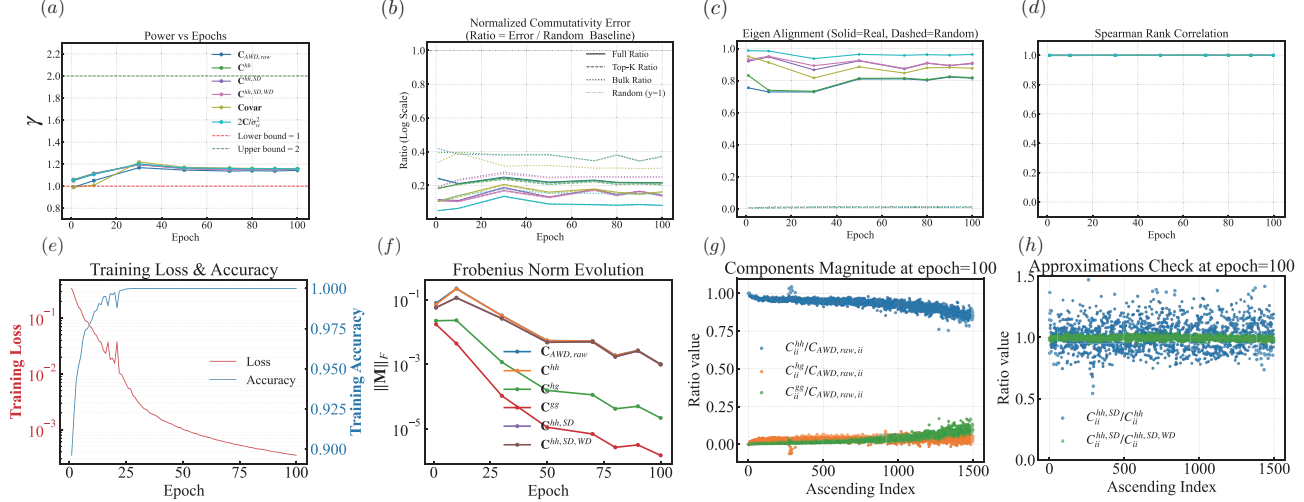


**Figure 4.** Comprehensive Analysis of SGD Noise Structure and Approximations (MLP on MNIST, CE Loss). **(a)** Evolution of the scaling exponent  $\gamma$ . The exponent  $\gamma$  remains robustly within the interval  $[1, 2]$  throughout training, it gradually increases as training progress and tends to deviate from the lower bound 1 when near the global minimum. Notably, in the terminal phase (near the global minimum, indicated by the vertical dashed line), the scaling exponent derived from the raw empirical covariance (**Covar**) converges to match both the AWD-derived covariance ( $\mathbf{C}_{AWD,raw}$ ) and its fully or partially approximations ( $\mathbf{C}^{hh}$ ,  $\mathbf{C}^{hh,SD}$ ,  $\mathbf{C}^{hh,SD,WD}$ ,  $\mathbf{C}^{hh,SD,WD,LI}$ , see E.2 for details), showing that the approximations used in Theorem 3.4 are valid. **(b)** Commutativity error between matrix pairs. The *Random* baseline (dash-dot line) represents the expected error ( $\approx 1.4$ ) for unrelated matrices. The significantly lower error for the covariances and Hessian indicates that they satisfy an approximate commutation relation. **(c)** Eigen Alignment, measured as the ratio of the diagonal magnitude to the total magnitude of  $\mathbf{C}$  in the eigenbasis of  $\mathbf{H}$ . High ratios indicate that  $\mathbf{C}$  is nearly diagonal in  $\mathbf{H}$ 's basis, further supporting approximate commutativity. **(d)** Spearman Rank Correlation between the diagonals of  $\mathbf{C}$  and  $\mathbf{H}$  in  $\mathbf{H}$ 's eigenbasis. A value of 1.0 indicates a strict monotonic correspondence between the noise and curvature spectra. **(e)** Training dynamics showing the loss and accuracy; the model converges to 100% training accuracy around epoch 30. **(f)** Evolution of Frobenius norms validating the gradient noise approximation, see E.2 for the definition of these variables. The dominance of the Hessian-weight term ( $\mathbf{C}^{hh}$ ) over the gradient-activity terms ( $\mathbf{C}^{hg}$ ,  $\mathbf{C}^{gg}$ ) confirms the “Vanishing Gradients” assumption near the global minimum. The convergence of terms ( $\mathbf{C}_{AWD,raw}$ ,  $\mathbf{C}^{hh}$ ,  $\mathbf{C}^{hh,SD}$ ,  $\mathbf{C}^{hh,SD,WD}$ ) validates the *Independence of Distinct Samples* and *Local Isotropy* assumptions in Theorem 3.4. **(g)** Diagonals magnitude of ( $\mathbf{C}^{hh}$ ,  $\mathbf{C}^{hg}$ ,  $\mathbf{C}^{gg}$ ) compared to  $\mathbf{C}_{AWD,raw}$  at epoch 100 (near the global minimum) vs. descending basis index, providing a detailed view of the dominance of the Hessian term ( $\mathbf{C}^{hh}$ ). **(h)** Diagonals magnitude of ( $\mathbf{C}^{hh}$ ,  $\mathbf{C}^{hh,SD,WD}$ ) compared to  $\mathbf{C}^{hh,SD}$  at epoch 100 (near the global minimum) vs. descending basis index, further confirming that the independence and isotropy assumptions hold near the global minimum.

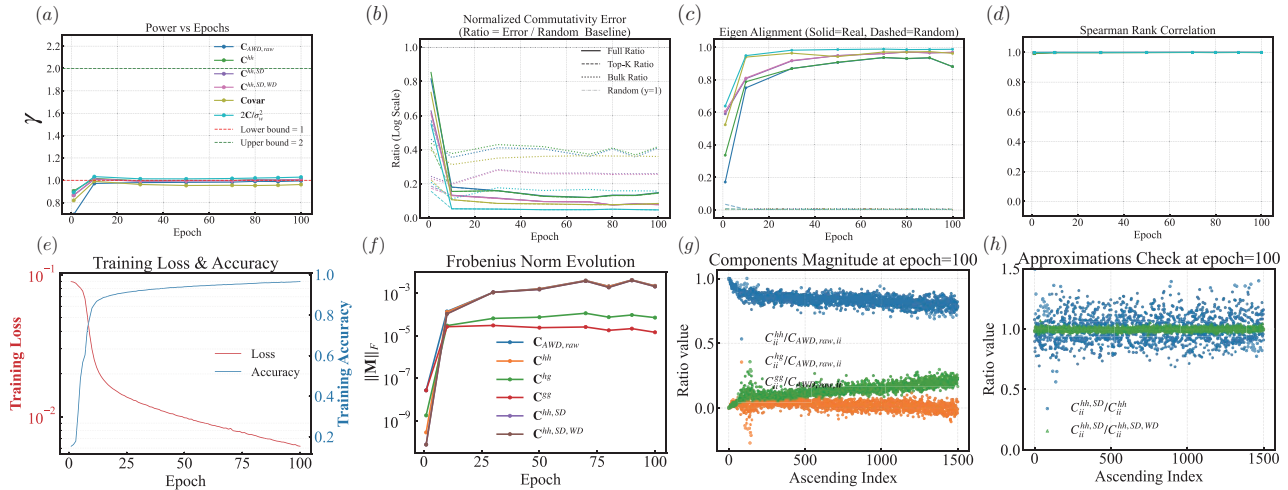


**Figure 5.** Comprehensive Analysis of SGD Noise Structure and Approximations (MLP on MNIST, MSE Loss) **(a)** Different from the case with CE loss, the exponent  $\gamma$  remains 1 when the model is near the global minimum.

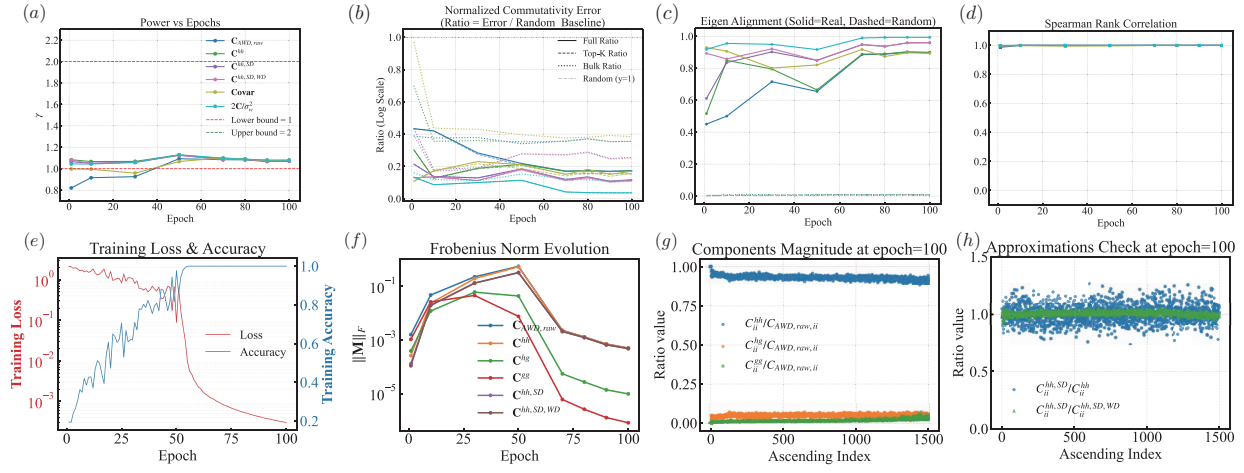
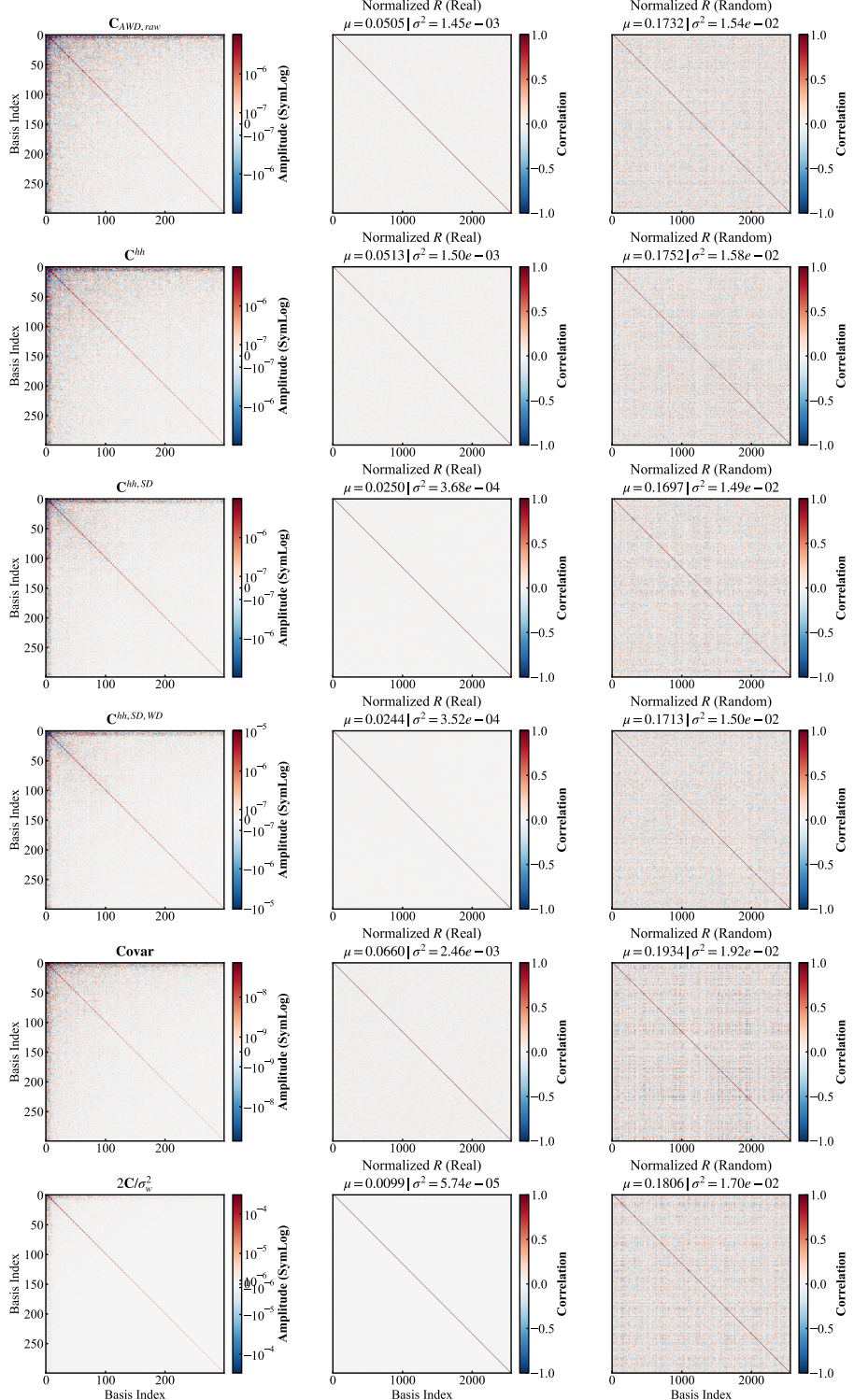


Figure 6. Comprehensive Analysis of SGD Noise Structure and Approximations (CNN on CIFAR-10, CE Loss)

(a) The exponent  $\gamma$  gradually increases as the training progress and shows significant deviation from the lower bound 1 when the model is near the global minimum.



**Figure 7.** Visualization of Noise-Curvature Alignment (CNN on CIFAR-10 with CE loss, trained to convergence with 100% training accuracy). The first column shows the Empirical Covariance Matrix Covar, AWD-derived  $C_{AWD, raw}$ ,  $C^{hh, SD}$ ,  $C^{hh, SD, WD}$ ,  $C^{hh}$  and  $2C/\sigma_w^2$  in the Hessian eigenbasis which consistently show arrowhead structures. The second column shows the corresponding normalized Correlation Matrix  $\mathbf{R}$  for real data, which is strongly diagonal (red diagonal on bright background), indicating precise geometric alignment. The third column shows the randomized baseline  $\mathbf{R}_{\text{rand}}$  (where  $\mathbf{C}$  is randomly rotated) resembles “static noise,” showing that without alignment, energy leaks across all dimensions.  $\mu$  and  $\sigma^2$  represent the mean value and variance of the absolute values of off diagonal elements.

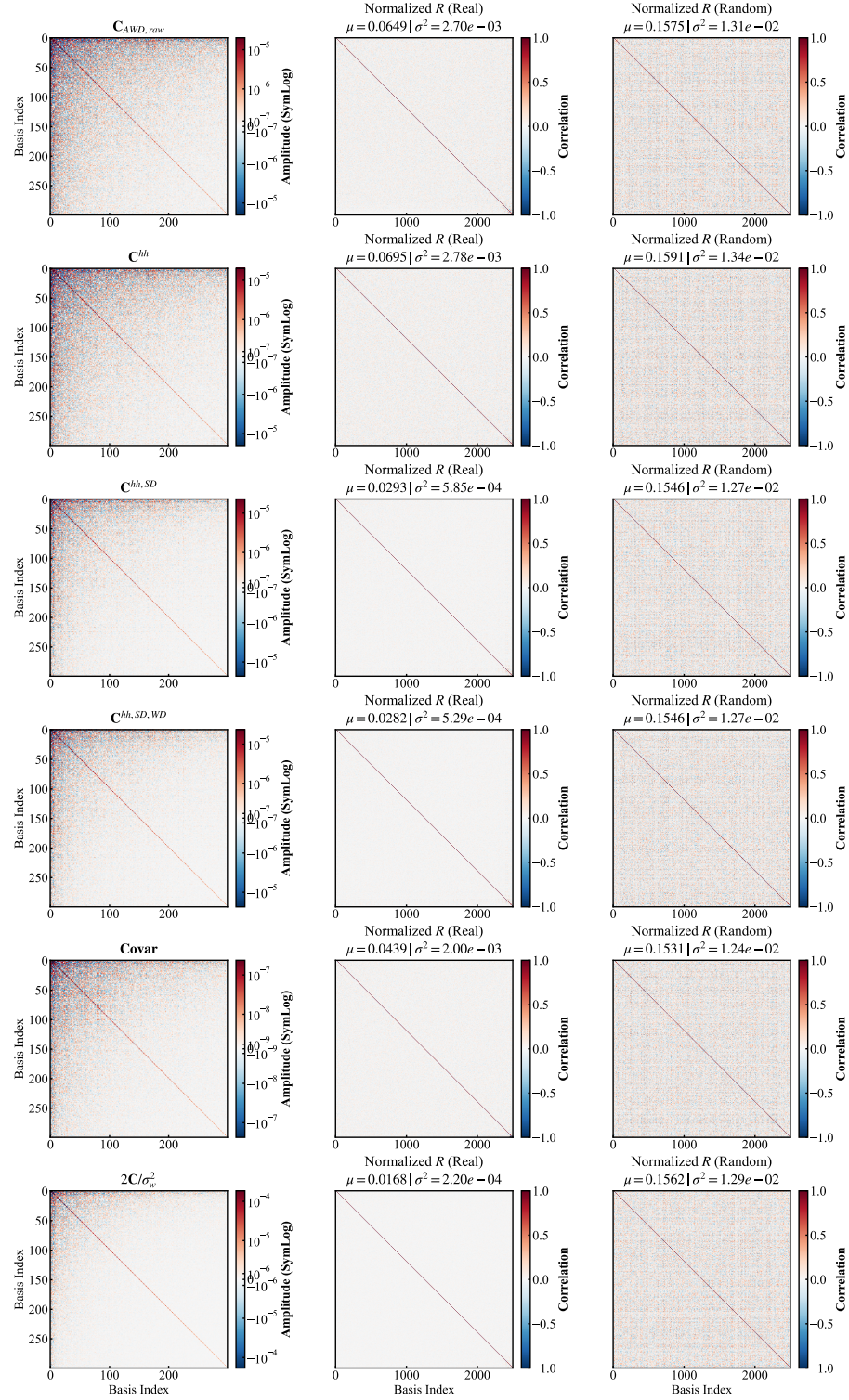


Figure 8. Visualization of Noise-Curvature Alignment (MLP on MNIST with CE loss, trained to convergence with 100% training accuracy).

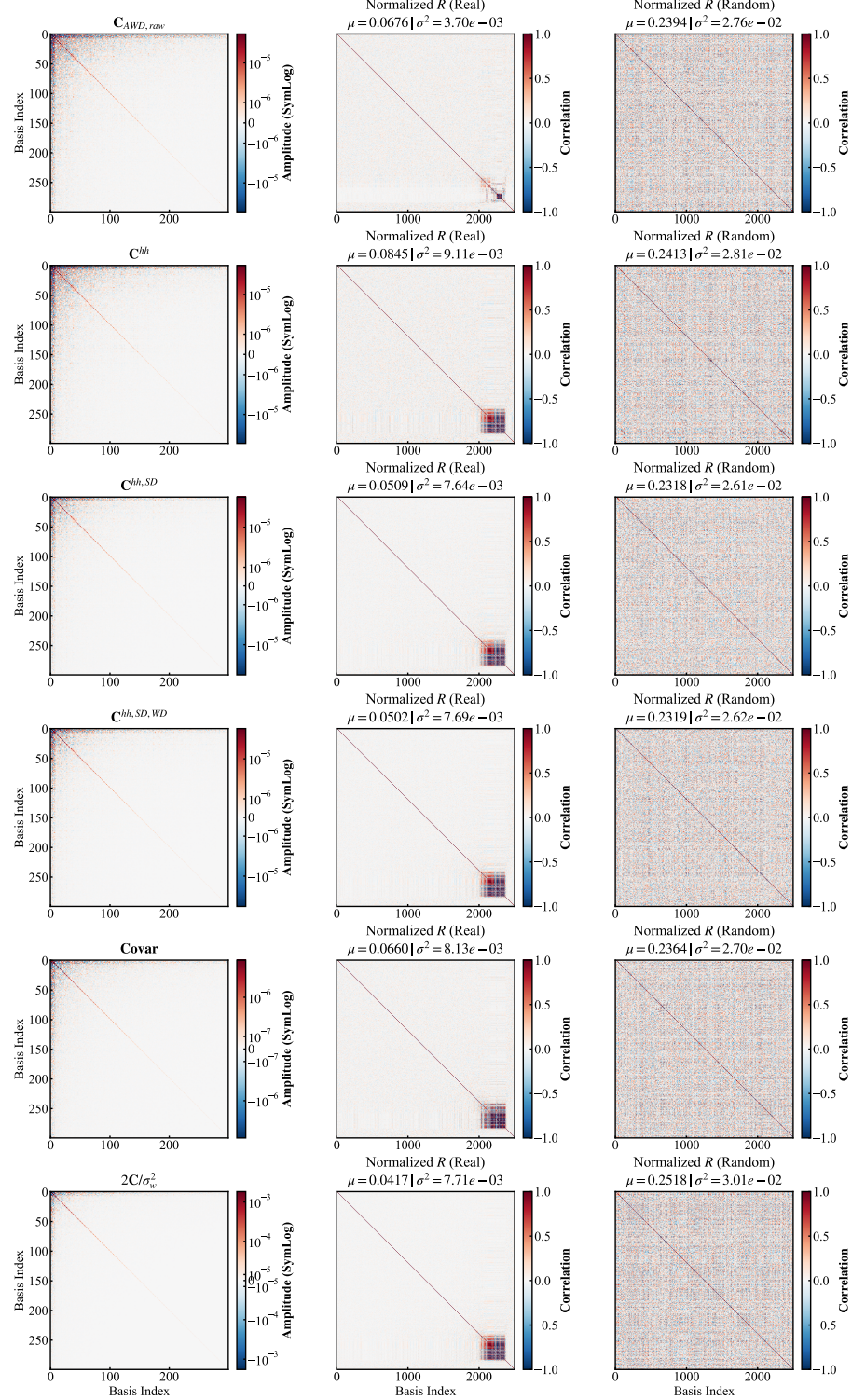


Figure 9. Visualization of Noise-Curvature Alignment (MLP on MNIST with MSE loss, trained to approach  $\sim 95\%$  training accuracy). The dark block in the second column originates from the degenerated spectrum where the eigenvalues are too small for these flatter direction.

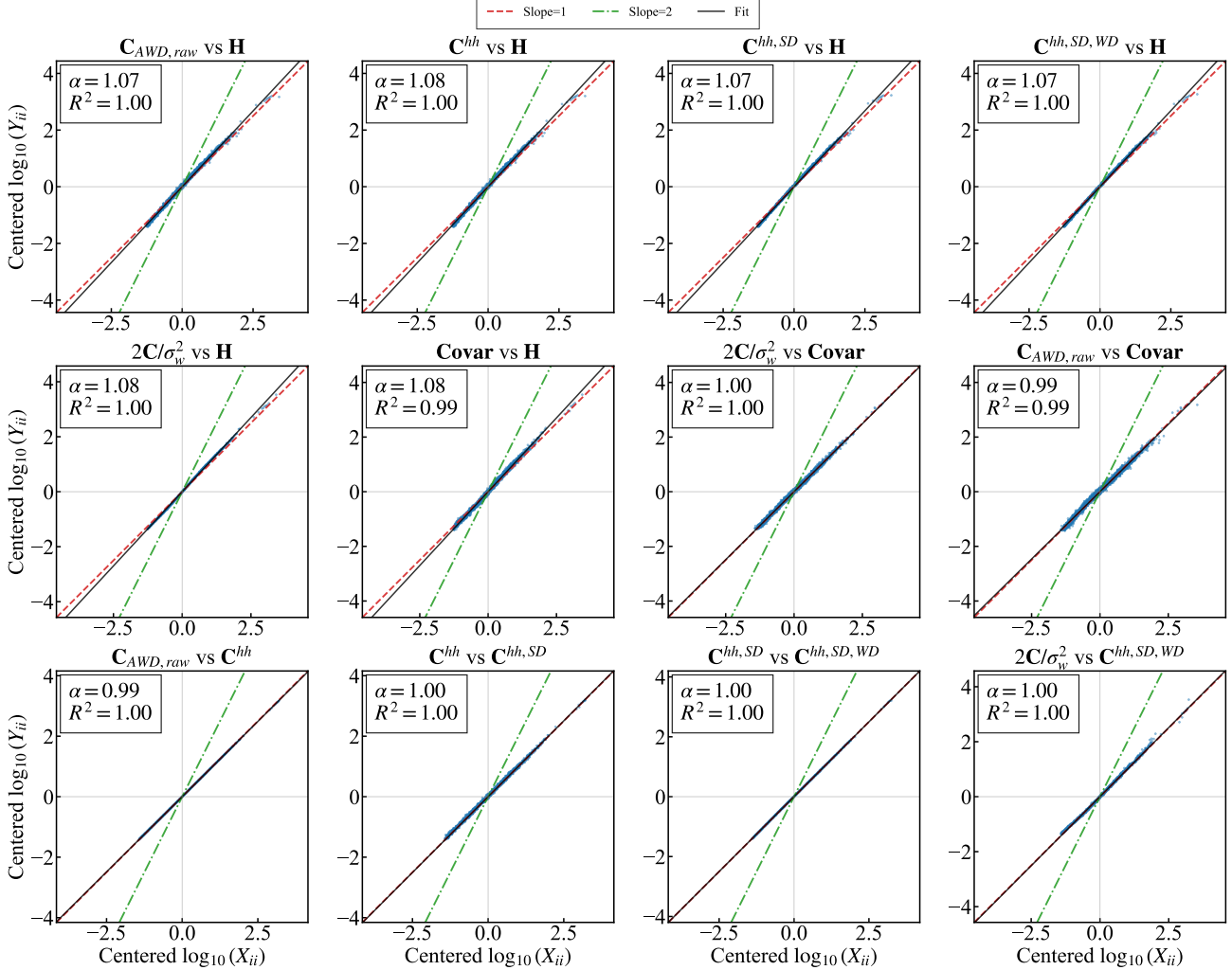


Figure 10. Log-log scaling analysis of diagonal elements (Top  $\mathcal{N} = 1500$  eigenvalues) for models trained to convergence 100% training accuracy (CNN on CIFAR-10 with CE loss). To isolate the scaling exponent  $\gamma$  (slope) from magnitude differences, data (dots) are mean-centered; solid lines indicate linear fits. Despite differences in magnitude, the centered log-log plots comparing the Empirical Covariance **Covar**, Hessian **H**, and AWD-derived Covariance  $2\mathbf{C}/\sigma_w^2$  (including approximations  $\mathbf{C}_{AWD,raw}$ ,  $\mathbf{C}^{hh}$ ,  $\mathbf{C}^{hh,SD}$ ,  $\mathbf{C}^{hh,SD,WD}$ ) demonstrate the validity of our theory and the accuracy of the employed approximations.

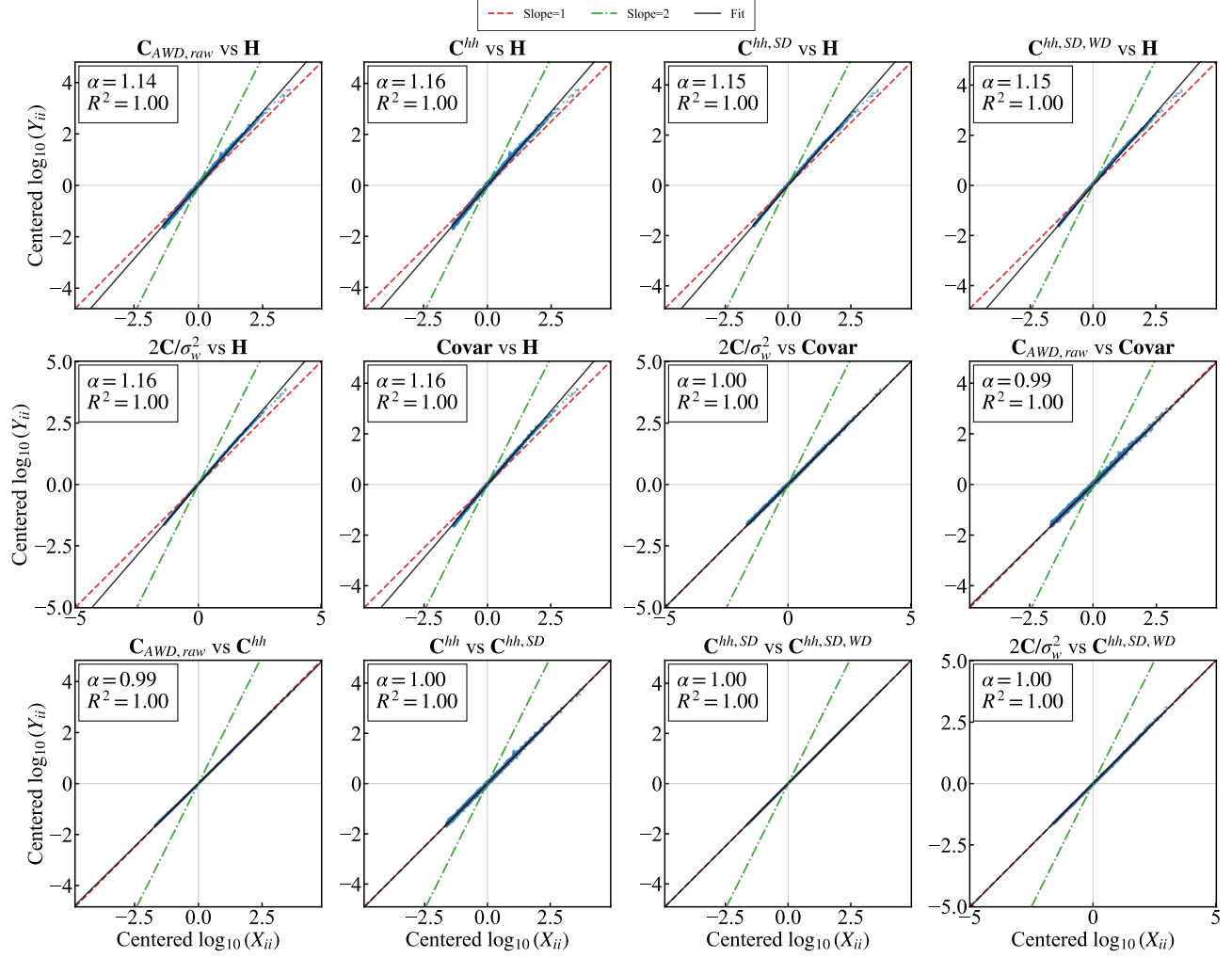


Figure 11. Log-log scaling analysis of diagonal elements (Top  $\mathcal{N} = 1500$  eigenvalues) for models trained to convergence 100% training accuracy (MLP on MNIST with CE loss).

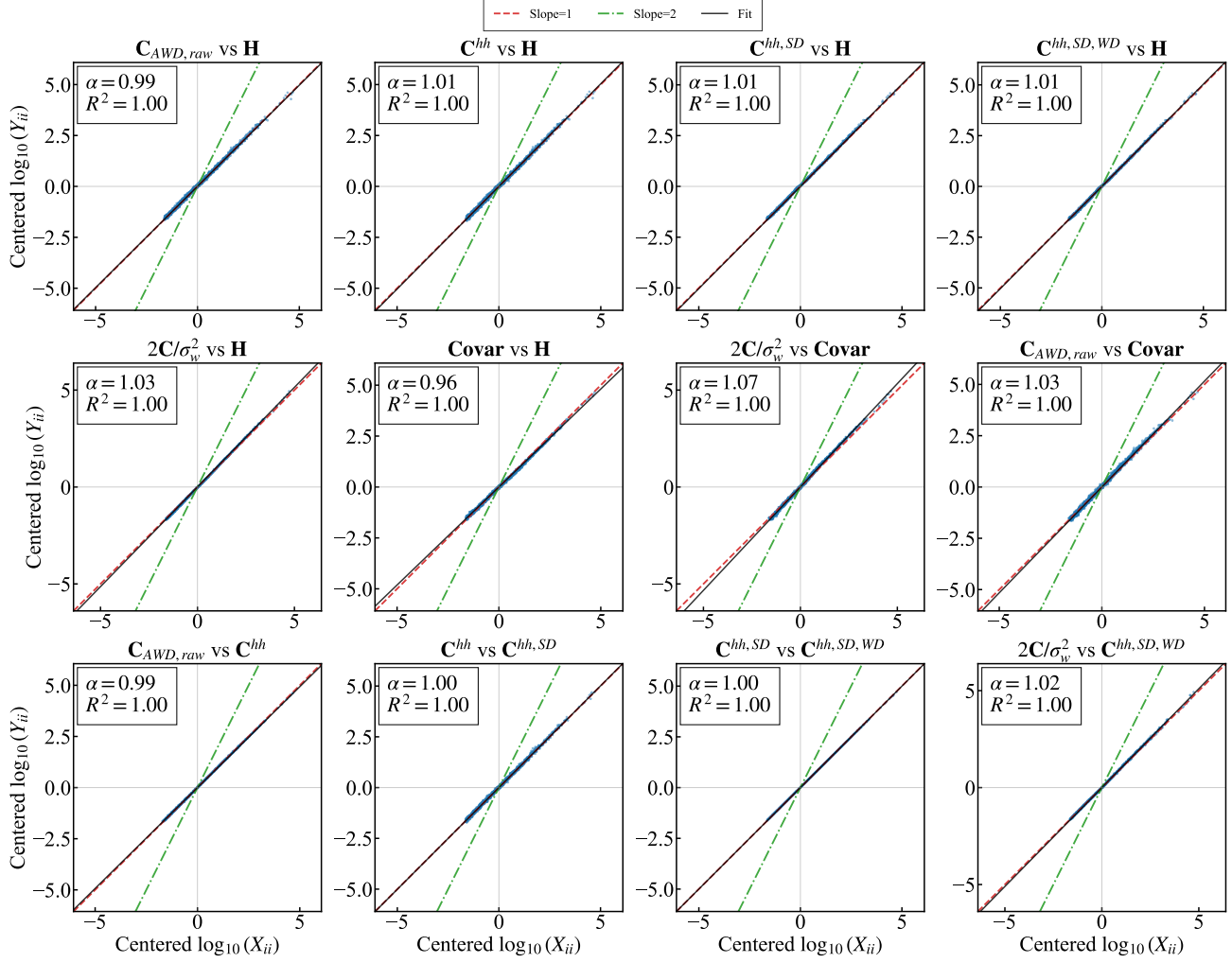
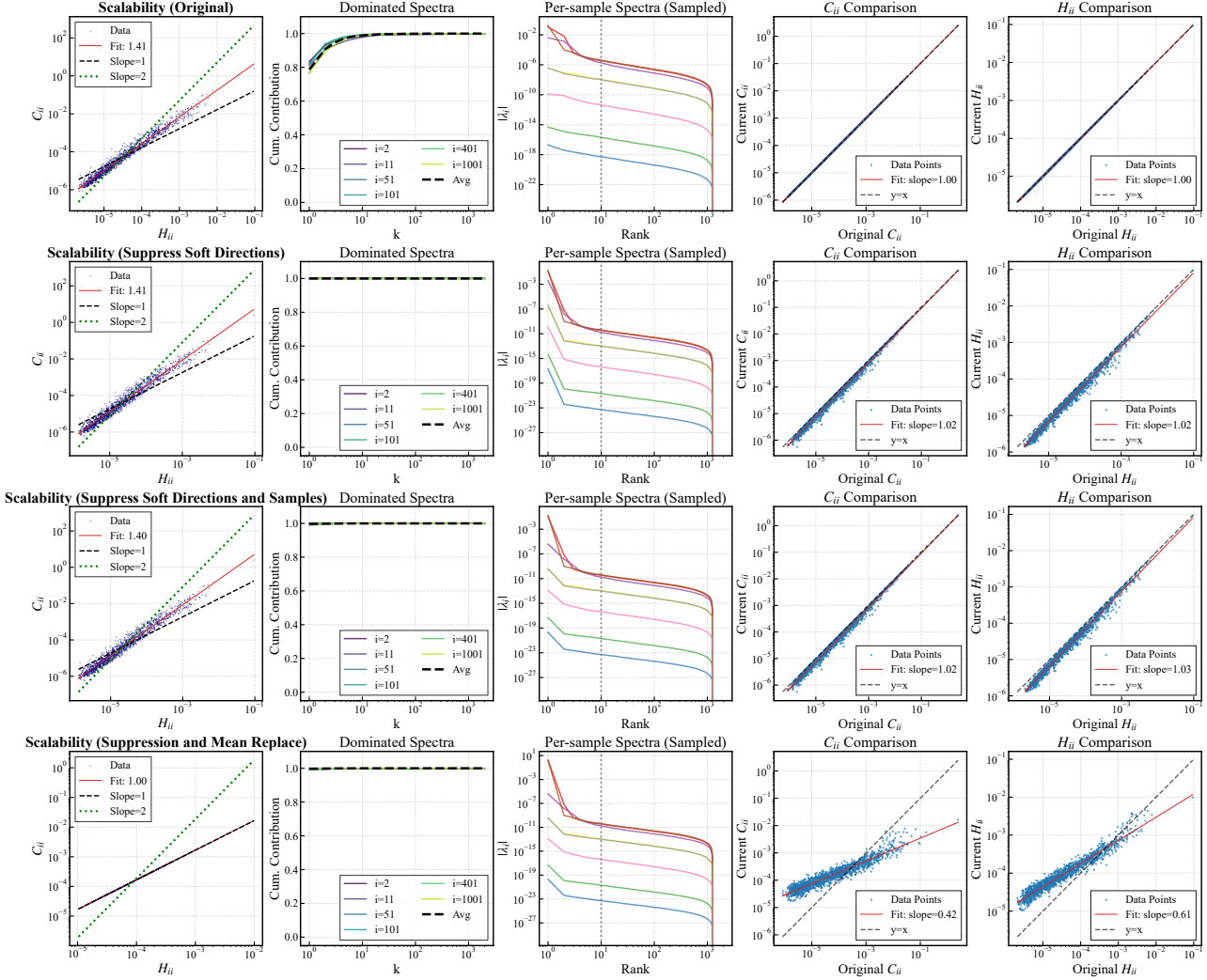


Figure 12. Log-log scaling analysis of diagonal elements (Top  $\mathcal{N} = 1500$  eigenvalues) for models trained to convergence 100% training accuracy (MLP on MNIST with MSE loss).



**Figure 13.** “Suppression experiment” for MLP on CIFAR-10 with CE loss ( $\gamma \sim 1.4$  significantly larger than 1). The 1st column shows the log-log plot of diagonals between  $2C_{ii}/\sigma_w^2 = \mathbb{E}_p \left[ \sum_m (\kappa_m^{(p)})^2 (\mathbf{u}_m^{(p)} \cdot \mathbf{v}_i)^2 \right]$  and  $H_{ii} = \mathbb{E}_p \left[ \sum_m (\kappa_m^{(p)}) (\mathbf{u}_m^{(p)} \cdot \mathbf{v}_i)^2 \right]$ , while each row corresponds to different revised per-sample spectra. The 2nd column shows the cumulated contribution of per-sample eigenmode  $\kappa_k^{(p)}$  defined by  $\mathbb{E}_p \left[ \sum_{m=1}^k (\kappa_m^{(p)})^2 (\mathbf{u}_m^{(p)} \cdot \mathbf{v}_i)^2 \right] / \mathbb{E}_p \left[ \sum_m (\kappa_m^{(p)})^2 (\mathbf{u}_m^{(p)} \cdot \mathbf{v}_i)^2 \right]$  for different global hessian eigen-directions  $i \in [1, N]$ , where the bold black dashed line is the average among  $i$ . It is obvious that the first stiff mode contributes  $> 80\%$ . The 3rd column shows the per-sample hessian spectra before (the first row) and after (the rest rows) revision. The 4th and 5th columns show the log log plot of the diagonals between the raw and cooked  $2C_{ii}/\sigma_w^2$  and  $H_{ii}$  generated by original and revised per-sample hessian spectra separately. The 1st row shows the case where the per-sample hessian remains unchanged. The 2nd row shows the case keeping the first stiff eigenvalue  $\kappa_1^{(p)}$  unchanged while suppressing the rest (scaling by  $1e-5$ ). In this case,  $2C_{ii}/\sigma_w^2$  and  $H_{ii}$  hardly change. For the 3rd row, based on the manipulation in the 2nd row, we further suppress the contribution (scaling by  $1e-3$ ) of non-stiff samples for those with  $\kappa_1^{(p)} < \theta \max_p \kappa_1^{(p)}$ , here we set the threshold  $\theta = 0.001$  that keeps 36 out of 200 total samples. In this case,  $2C_{ii}/\sigma_w^2$  and  $H_{ii}$  hardly change. For the last row, we replace the remaining  $\kappa_1^{(p)}$  to their mean value.  $2C_{ii}/\sigma_w^2$  and  $H_{ii}$  change significantly, yielding  $\gamma = 1$ .

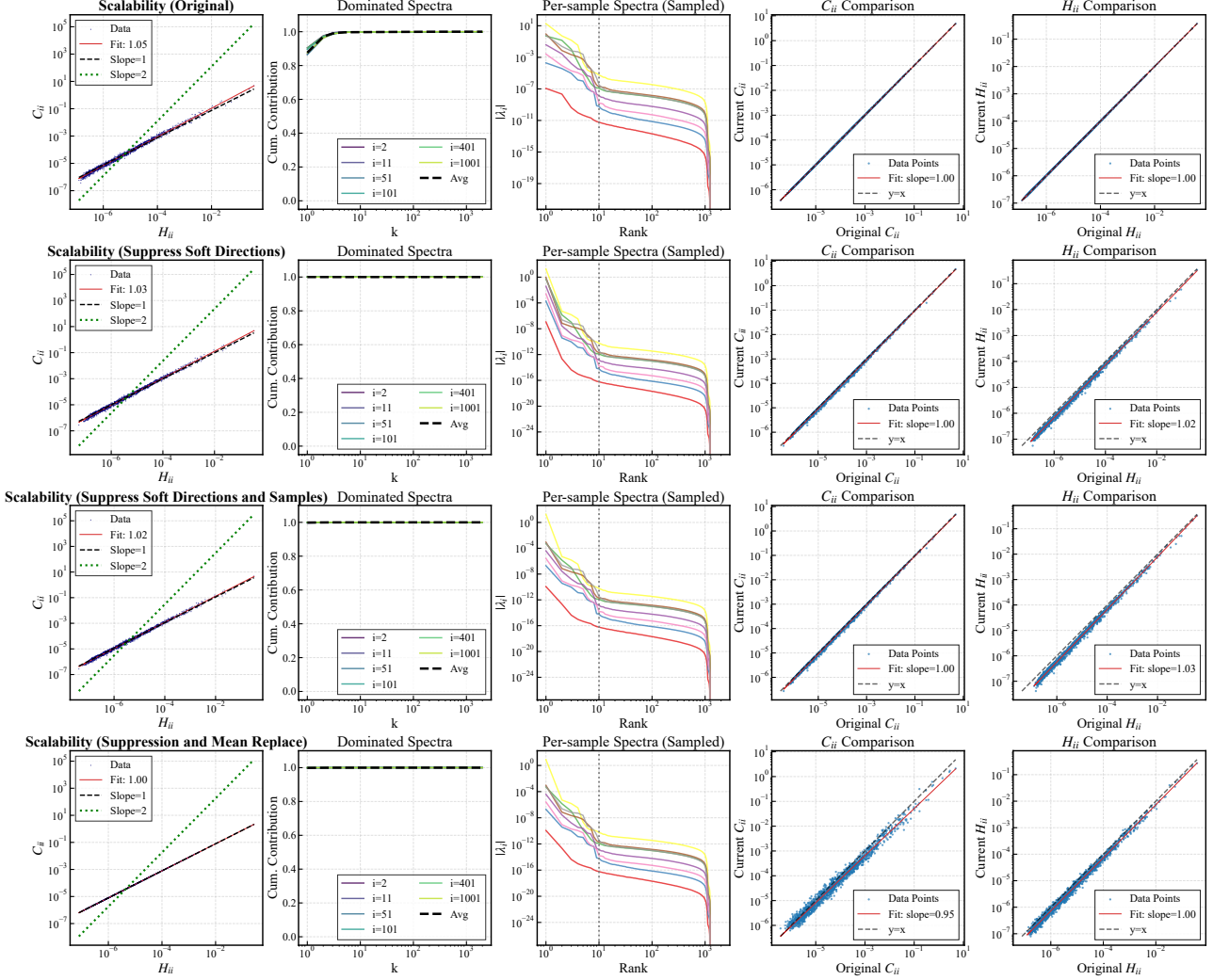


Figure 14. “Suppression experiment” for MLP on MNIST with MSE loss ( $\gamma \sim 1.05$  near to 1). Similar to Figure 15, here the threshold  $\theta = 0.05$  and keeps 33 stiff samples out of 200. Compared to the raw data, cooked  $2C_{ii}/\sigma_w^2$  and  $H_{ii}$  slightly change but keep the linear scaling.

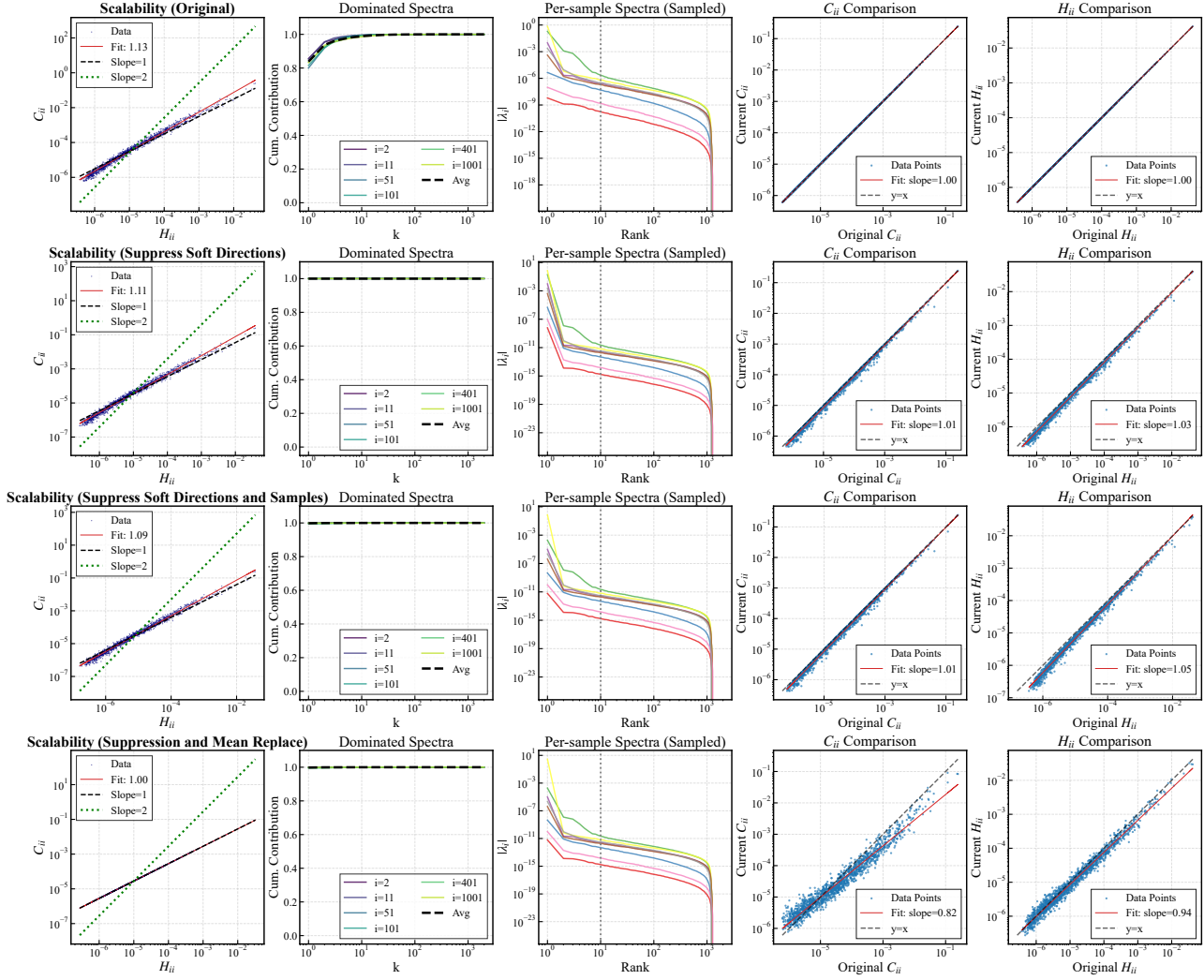


Figure 15. “Suppression experiment” for MLP on MNIST with CE loss ( $\gamma \sim 1.1$  slightly larger than 1). The threshold  $\theta = 0.05$  and keeps 20 stiff samples out of 200. Compared to the raw data, cooked  $2C_{ii}/\sigma_w^2$  and  $H_{ii}$  changes to some extend.